Partial coupling and earthquake potential along the Xianshuihe Fault, China

Yuexin Li[1] and Roland Bürgmann[1]

[1] Department of Earth and Planetary Science and Berkeley Seismology Laboratory, University of California, Berkeley, CA, USA.

Corresponding author: Yuexin Li (yuexinli@berkeley.edu)

Key Points:

- Obtained high-resolution velocity maps along the Xianshuihe Fault using ascending and descending Sentinel-1 interferograms from 2014 to 2019
- InSAR constrained coupling model along the fault indicates high earthquake potential
- Identified multiple shallow creeping patches along the fault and substantial afterslip near the 2014 Kangding earthquake rupture

Abstract

The left-lateral Xianshuihe Fault is located at the eastern boundary of the Tibetan Plateau and is one of the most active faults in China. It is associated with substantial seismic potential, with more than 20 Mw>6 earthquakes since 1700. The fault has been documented to be creeping at the surface for decades; however, the spatial and temporal distributions of shallow creep along the fault are not well resolved. In this study, we obtain high-resolution interseismic velocity maps along the 350-km-long central Xianshuihe Fault and Interferometric Synthetic Aperture Radar (InSAR) timeseries along the Kangding segment using ascending and descending Sentinel-1 data. The InSAR data reveal multiple creeping sections and the estimated surface creep rates show high along-strike variability. A coupling model characterizes the distribution of creep with depth. The seismic potential of apparent rupture asperities along the Xianshuihe Fault is further refined by considering fault-crossing baseline data and the distribution of historical ruptures and microseismicity. Moreover, a stress-driven afterslip model of the observed accelerated creep around the Mw 5.9 2014 Kangding rupture indicates substantial shallow afterslip, which provides further constraints on the distribution of locked and creeping patches along this section of the Xianshuihe Fault.

1 Introduction

Creeping faults slip aseismically in their upper few kilometers and have been observed in various kinds of tectonic settings and environments around the world (Harris, 2017; Bürgmann, 2018). Continental strike-slip creeping faults represent an important portion of the slow slip family. In addition to field deployed creepmeters, alignment arrays and near-field GPS measurements, the dense spatial sampling of InSAR has proved to be particularly valuable for studies of creeping strike-slip faults, such as the San Andreas Fault (e.g. Tong et al., 2013) and the Hayward-Calaveras fault zone (e.g. Chaussard et al., 2015) in California, the Haiyuan Fault (e.g. Jolivet et al., 2012) in China, and the North Anatolian Fault (e.g. Aslan et al., 2019) in Turkey. Spatiotemporal variations of fault creep rates can be linked to the spatial distribution of locked fault sections and the occurrence of nearby earthquakes (e.g. Jolivet et al., 2012; Shirzaei & Bürgmann, 2013; Khoshmanesh et al., 2015).

Even though there is little interseismic strain accumulation along the uppermost part of rapidly creeping faults, destructive earthquakes can still occur on these faults to compensate for the slip deficit accumulating on coupled portions of the fault at greater depth over time. However, due to limited observations available, the mechanisms and dynamics of fault creep still remain unclear. Regarding what makes a fault creep, several possible explanations have been proposed, including specific fault zone materials that have low frictional resistance and rate-strengthening properties (e.g., serpentinite found near creeping faults in California, Harris, 2017), elevated pore pressure in the fault zone that reduces the effective normal stress (e.g., Superstition Hills Fault in California, Wei et al., 2009), and the response to static and/or dynamic stress changes from nearby earthquakes (e.g., the North Anatolian Fault, Çakir et al., 2012). In the context of regional seismic hazard evaluation, a better characterization of creeping faults can also help map out the distribution of locked and creeping patches on the fault that can be incorporated into rupture and ground motion modeling (e.g., Aagaard et al., 2012).

The left-lateral Xianshuihe Fault (XSF) is located at the eastern boundary of the Tibetan Plateau (Figure 1), which is one of the bounding faults that accommodates the distributed convergence of

the Indian and Eurasian plates (Zhang, 2013). Being one of the most active faults in China, the Xianshuihe Fault is associated with substantial seismic potential. Since 1700, more than 20 M_w > 6 earthquakes occurred along the Xianshuihe Fault (Wang et al., 2009; Bai et al., 2018), including the 1973 M_s 7.4 Luhuo earthquake, the 1981 M_s 6.8 Daofu earthquake (Wen et al., 2008), and the most recent 2014 M_w5.9 Kangding earthquake doublet (Jiang et al., 2015a) (Figure 1).

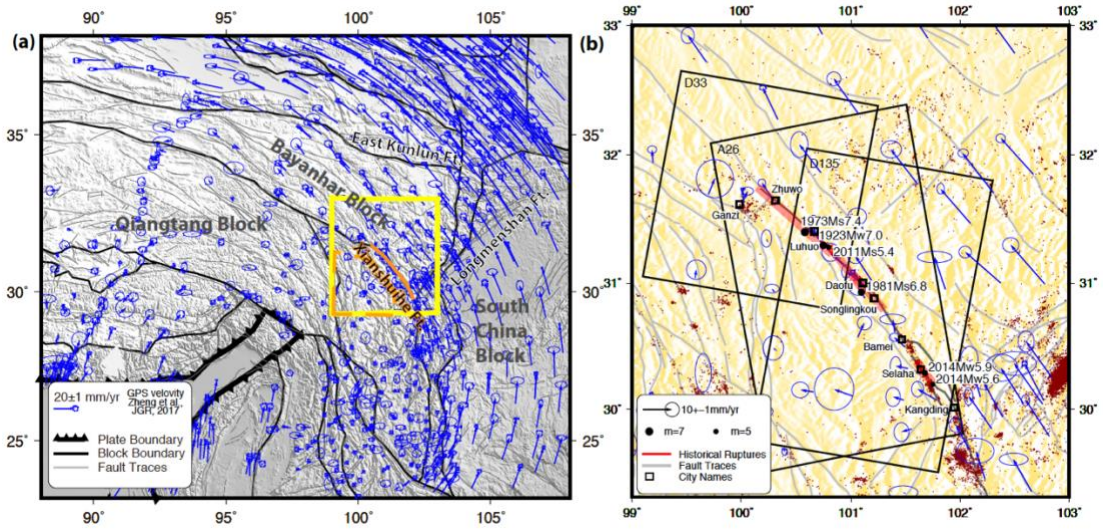

Figure 1. (a) Overview map of active crustal deformation across the Tibetan Plateau. The study region is indicated by the yellow rectangle. Blue arrows show GPS velocities tipped with 95% confidence ellipses measured during 1991–2015 (Zheng et al., 2017) referenced to the Yajiang sub-block. The Euler pole of the Yajiang block (angular rotation of lon/lat/w= [95.194°E, 24.8°N, -1.409°/Myr] with respect to Eurasia) is determined from GPS station velocities within the region outlined by orange dashed lines. (b) A zoom-in map of the Xianshuihe Fault region. Black boxes show the Sentinel-1 SAR coverage for ascending track 26 and descending tracks 33 and 135. Historical earthquakes and their ruptures are labeled along the fault. Dark red circles show regional M≥1.5 seismicity from China Seismic Experiment Site (2009-2019; Wu et al., 2019) and grey fault lines are from Xu et al. (2016).

Geological studies found its late Quaternary slip rates to be ~10 mm/yr (Bai et al., 2018) consistent with the geodetic slip rate inferred from 25 years (1991–2015) of GPS measurements (Zheng et al., 2017). Regarding recent InSAR studies, Wang et al. (2009) first obtained a velocity map using data from the ERS-1/2 and Envisat satellites acquired between 1996 and 2008, and inverted for a 9~12 mm/yr slip rate on a buried screw dislocation with a shallow 3-6 km locking depth along the northwestern XSF. Zhang et al. (2019) obtained a velocity map using Sentinel-1A data between December 2014 and November 2016 showing evidence of creep on the fault. Moreover, Zhang et al. (2018) used more than 30 years of fault-crossing short-baseline and short-leveling surveys since 1976 to show the surface creep and slip behavior at seven sites along the XSF. The largest surface creep occurred near the 1973 Luhuo earthquake rupture, reflecting decaying surface slip rates

following this event. However, details of the distribution of creep in space and time have not yet been resolved.

To characterize fault creep at and below the Earth's surface, dense and accurate measurements of crustal deformation in both the near field and far field are crucial. The dense sampling of InSAR and its global coverage make it a unique geodetic tool that we can leverage in areas that lack dense GPS coverage. The launches of Sentinel-1A in 2014 and Sentinel-1B in 2016 effectively reduced the satellites' recurrence intervals to as little as 6 days, making interseismic deformation and its temporal variation possible to resolve in a relatively short time period. However, there are still substantial challenges for InSAR observations of creeping faults, given that the interseismic signals tend to be relatively subtle (~mm/yr) and are often contaminated by atmospheric noise.

Therefore, in this study, we aim to find optimal InSAR processing schemes that focus on retrieving the subtle interseismic signals as well as characteristics of surface creep along the XSF. As the recent Kangding earthquake occurred just after the launch of Sentinel-1, we also seek to quantify the aseismic fault slip response to the seismic event, and to assess how such seismic events interact with the interseismic fault creep.

2 Data and Methods

2.1 InSAR data and processing

The InSAR data are processed using the GMTSAR software (Sandwell et al,. 2011 a, b). We use data from two Sentinel-1 descending tracks (135, 33) and one ascending track (26) covering the study region. The spatial coverage of the Sentinel-1 data is shown in Figure 1(b). All available (254) images from December 2014 to August 2019 are considered to estimate interseismic velocities and time series, excluding scenes collected before the 2014 M_w5.9 Kangding earthquake to separate out the coseismic offsets. More detailed information about the available interferograms can be found in Table 1.

Table 1. Sentinel-1 InSAR data after the 2014 Kangding earthquake sequence generated in this study.

Tracks	Orbit	# Scenes	# Intf	Time span	# Intf selected
T135	Descending	57	340	20141213-20190720	13
T33	Descending	95	1090	20141218-20190713	14
T26	Ascending	102	1174	20141206-20190713	21

** # Intf: the number of all available interferograms generated in this study*

** # Intf selected: the number of interferograms that are selected to form the average velocity map*

Usually, the correlation between two SAR acquisitions will decrease with increasing time span due to the growth of vegetation, sediment transport, and extreme weather conditions. However, in some cases, interferograms spanning several years with small perpendicular baselines may have better performance than a much shorter-duration interferogram with an image contaminated by substantial atmospheric noise (e.g., wet or snowy season acquisitions). Therefore, to explore the optimal selection and combination of interferogram pairs for the velocity map formation, interferograms are produced based on a 2000-day temporal baseline threshold and 20-meter perpendicular orbit baseline threshold criteria. Baseline plots for all interferograms can be found in Figure S2. We decimate the interferograms to be 1 in every 16 pixels in range and 1 in 4 pixels

in azimuth direction, resulting in an image resolution of about 60×80 m. All interferograms are filtered using a 200-m Gaussian filter as well as an adaptive Goldstein filter (Goldstein & Werner, 1998). We masked all pixels with an average coherence lower than 0.09. Then, the masked interferograms are interpolated to assist in phase unwrapping using the Statistical-cost, Network-flow Algorithm for Phase Unwrapping software (SNAPHU, Chen & Zebker, 2002).

We found that average velocity maps generated from manually selected long-term interferograms with good signal-to-noise ratio work best for obtaining high-quality deformation observations in the XSF region compared with only using relatively short-term pairs. The selected interferograms are listed in Table S1 with the corresponding coherence and STD values of the unwrapped interferograms. Examples of selected interferograms that were used in the velocity map formation for each track, as well as some that were rejected, are shown in Figure 2 and Figure S3.

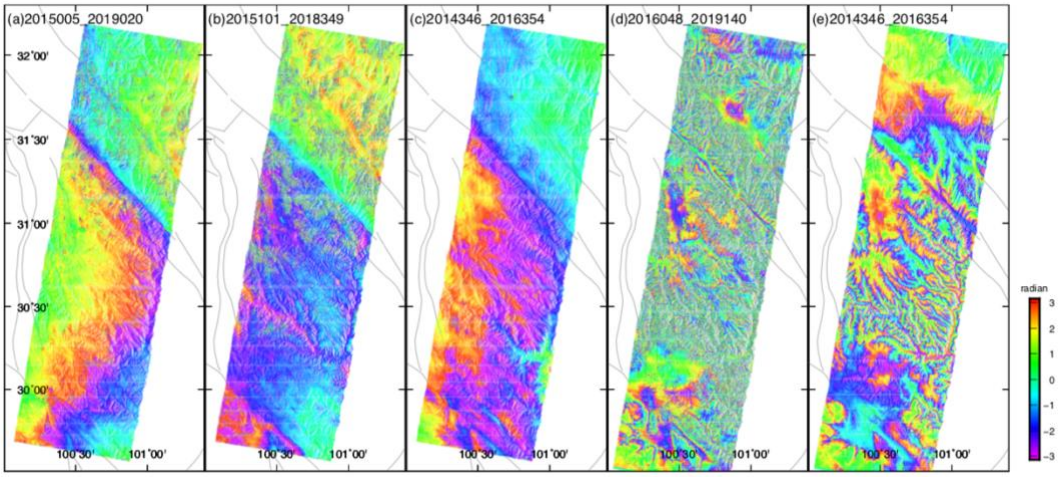

Figure 2. (a)-(c) Examples of selected good interferograms from descending track T135F3. (d)-(e) Examples of bad interferograms that are contaminated by decorrelation and topography-correlated atmospheric noise, respectively. Dates used to form the interferograms are shown at the top of each panel. See Figure S3 for additional examples.

Coseismic interferograms for the 2014 Kangding earthquake sequence

We use both ascending and descending Sentinel-1 interferograms to characterize the deformation field of the Kangding earthquake sequence. The coseismic interferograms used are 20141019-20141206 for track A26 and 20141026-20141213 for track D135. Baseline plots for the coseismic pairs are shown in Figure S2. The earthquake occurred ~7 months after the Sentinel-1A satellite launched. Luckily, the first available scenes covering the Kangding region along track A26 and D135 were acquired just before the earthquake. However, only one pre-earthquake scene is available and thus the atmospheric noise on that day contributing to the coseismic interferogram could not be suppressed by averaging multiple coseismic interferograms formed with different pre-earthquake scenes. We only applied a linear topography-correlated correction from the original

unwrapped interferograms to mitigate the effects of tropospheric delays. The original, unwrapped, and corrected interferograms for ascending and descending tracks are shown in Figure 3.

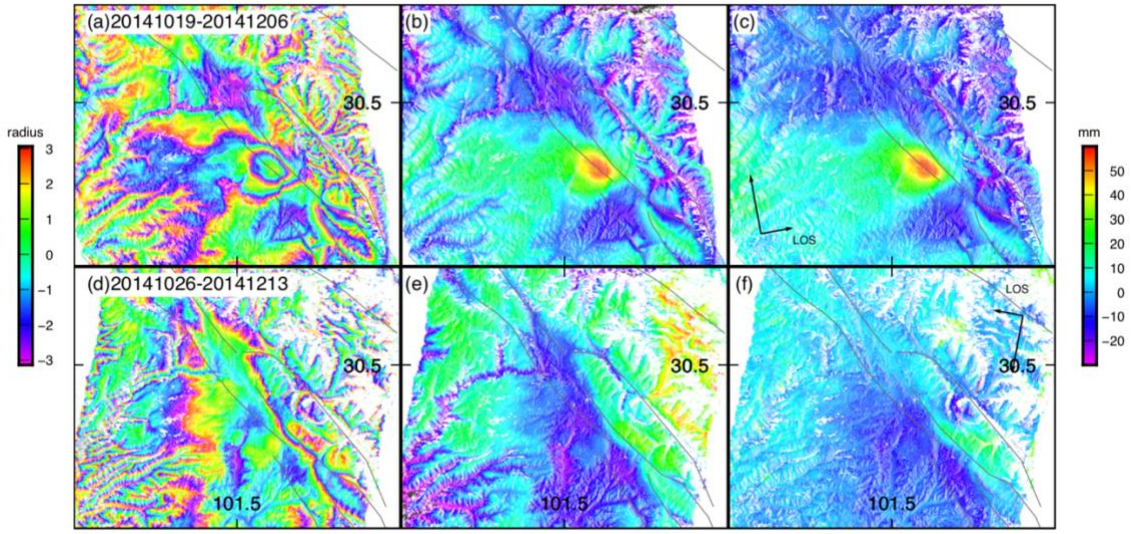

Figure 3. (a) Coseismic wrapped interferogram, (b) unwrapped interferogram and (c) interferogram after a linear topo-correlated atmospheric noise correction from ascending track 26. (d-f) Corresponding maps for descending track 135. Note that in (f), we also manually corrected for a clear unwrapping error (2pi) in the NE corner of the image.

Timeseries analysis using a subset of interferograms

To characterize the temporal behavior of fault creep along the XSF, more frequent temporal sampling of the SAR acquisitions is needed. We analyzed multiple properties of interferograms generated in Section 2.1 and found the manually selected interferograms used in the velocity map all have a relatively small standard deviation of unwrapped LOS change (STD) for the whole image (Figure S4). Accordingly, we selected from the generated interferograms with STD<3 to include a larger subset of interferograms (202) in the timeseries analysis. Due to the limited signal to noise ratio in the interferograms, we focus on the Kangding region in the timeseries analysis using descending track 135. The ascending track 26 are not used because the derived timeseries has a very low signal-to-noise ratio and no meaningful signal can be extracted. The interferograms that are used in the timeseries analysis are shown in Figure S2. Note that the interferograms used to produce the average velocity map in descending track 135 (Fig. 3b) represent a subset of the ones that were used in the timeseries analysis. More interferograms are included to ensure denser temporal sampling. The timeseries analysis is conducted using Small Baseline Subset method (SBAS; Berardino et al., 2002; Schmidt & Bürgmann, 2003). A linear regression between phase and topography was removed in each interferogram to reduce the effect of topography-correlated atmospheric noise.

2.2 Kinematic inversion for the seismic and aseismic fault slip

Kinematic inversions for both the coseismic and aseismic slip are conducted using the constrained least square methods. Green's functions relating unit slip on rectangular dislocations to range change or range change rate are calculated assuming a homogeneous elastic half-space (Okada,

1985). Laplacian smoothing is applied to avoid abrupt slip variations between neighboring patches. The inversion problem can be described as:

$$\binom{\boldsymbol{los}}{\mathbf{0}} = \binom{\boldsymbol{G}}{\boldsymbol{\lambda H^2}}\boldsymbol{m} \qquad \text{(Eq 1)}$$

where ***los*** represents the line of sight (LOS) range change measurements from the ascending and descending tracks, ***G*** is the Green's function matrix, H is the Laplacian smoothing matrix, $\boldsymbol{\lambda}$ is the smoothing factor and ***m*** is the slip vector for each fault patch that is being solved in the inversion. In this study, we only allow left-lateral strike slip for the slip vector ***m.***

3 Results

3.1 Average interseismic velocity map along the XSF

By stacking the manually selected interferograms listed in Table S1, we form average velocity maps for both ascending and descending tracks (Figure 4 a, b). The LOS velocities measured in the two SAR geometries have opposite signs across the XSF, indicating that the signal is dominated by horizontal strike-slip fault motion.

If we assume all horizontal motions to be fault parallel, the LOS velocity maps from ascending and descending looking geometries can be decomposed into fault-parallel velocities $\boldsymbol{u}$ and vertical velocities $\boldsymbol{w}$, where $\boldsymbol{\theta}$ is the average fault strike of the patch, and ($\boldsymbol{look_E}, \boldsymbol{look_N}, \boldsymbol{look_Z}$) are look vectors for each flight direction, respectively (Eq 2).

$$\binom{V_{los\_asc}}{V_{los\_des}} = \begin{pmatrix} look_{E\_asc}\sin\theta + look_{N\_asc}\cos\theta & look_{Z\_asc} \\ look_{E\_des}\sin\theta + look_{N\_des}\cos\theta & look_{Z\_des} \end{pmatrix}\binom{u}{w} \qquad \text{(Eq 2)}$$

However, the strike of the XSF increases from ~125° in the NW to ~160 ° in the SE. Due to such a significant change in strike, assuming a uniform strike for the velocity decomposition would bias the result. Thus, we divide the LOS velocity maps into three swaths shown in Figure 4 a, b. From NW to SE, the patch lengths are 80, 120 and 120 km, respectively. The average strike of each

patch is 129°,131° and 145°. All patches have 100 km widths, extending for 50 km on either side of the fault.

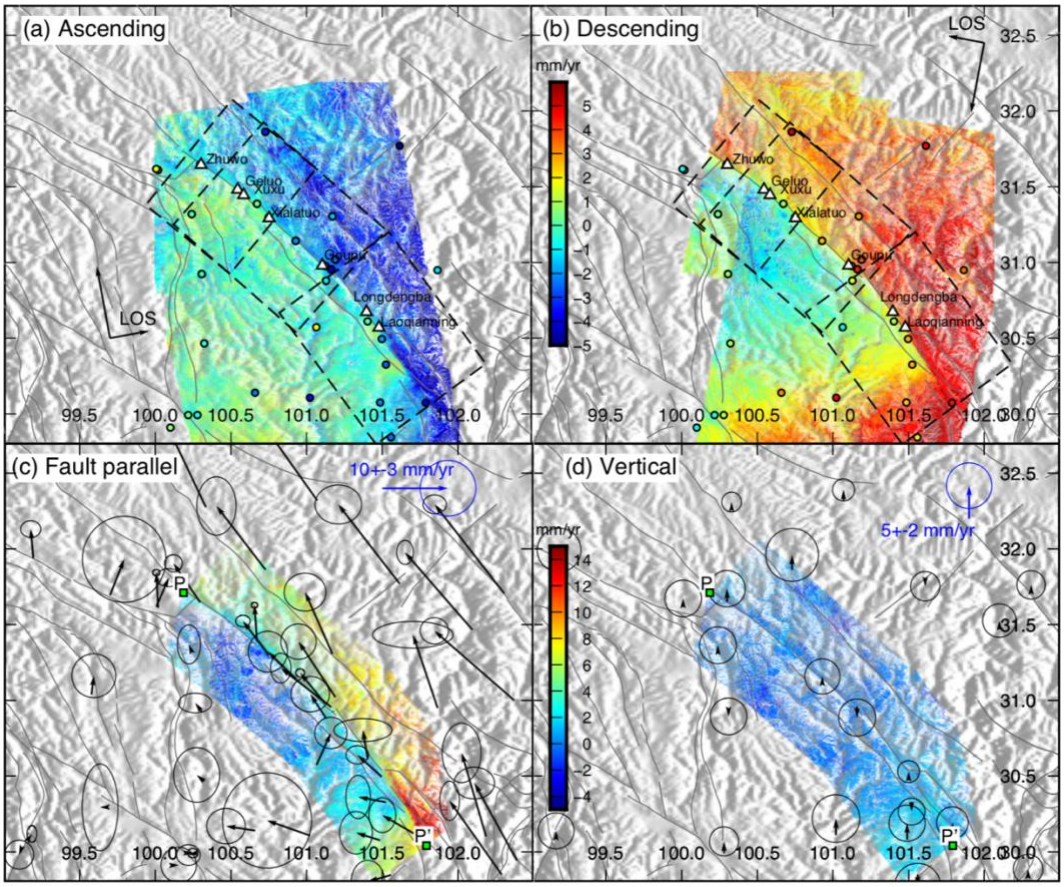

Figure 4. (a), (b): Average LOS velocity maps for (a) ascending track 26 and (b) descending tracks 33 and 135 in the Xianshuihe Fault region. In both (a) and (b), red color represents radar range increase and blue color represents range decrease. Fault-crossing baseline survey sites from Zhang et al. (2018) are denoted with yellow triangles labeled with their station names. Co-registered and projected LOS velocities from GPS measured horizontal velocities from Zheng et al. (2017) are shown with circles using the same color scale. InSAR and GPS velocities are referenced to the Yajiang sub-block (Figure 1). (c)(d): Decomposed velocity maps of (c) fault-parallel and (d) vertical components. In (c), red coloring represents SE motion and blue indicates NW motion. GPS vectors are horizontal GPS velocities from Zheng et al. (2017) referenced to regional Yajiang sub-block. In (d), blue represents uplift and red represents subsidence. GPS vectors are vertical GPS velocities from Liang et al., (2013). We subtract 1.41 mm/yr of uplift from the original GPS velocities in the ITRF2008 reference frame to highlight local uplift-rate variations (Liang et al., 2013).

This allows us to obtain velocity maps of fault-parallel and vertical components using the average strike of the corresponding patch, assuming that all horizontal motions are parallel to the corresponding fault segment (Figure 4 c, d). The inferred fault-parallel velocity difference across the fault of 10-12 mm/yr between areas ~50 km away from the fault trace is generally consistent with GPS measurements (Figure 4c) and geologic slip-rate studies (Zheng et al., 2017; Bai et al.,

2018). No significant vertical motion was observed. The decomposed vertical velocities range from 0-2 mm/yr, which is consistent with the vertical GPS solution by Liang et al. (2013) (Figure 4d).

3.2 Along-strike variation of the creep rate

With the high-resolution average velocity map along the XSF, we first manually mapped the active fault trace of the XSF within the SAR coverage by finding the maximum InSAR velocity gradient and considering published fault trace maps and the regional morphology in Google Earth. Then, we estimate surface creep rates along the fault trace by drawing fault-normal velocity profiles every 2 km along the fault, where each profile includes data from a 2-km wide zone. We explored multiple choices of profile lengths on either side of the fault that are used to estimate surface creep and compared results using alternative estimation methods (Text S1). In our preferred approach, the profiles extend for 1.5 km on either side of the fault. The pixels within 0.5 km of the fault trace are masked out to allow for uncertainties of the assumed fault location. Thus, only the velocity of pixels between 0.5-1.5 km from the fault on each side are used in the creep rate estimation. For each profile, we did a linear regression to fit a straight line on each side of the fault. Then, we calculate the modeled velocity at the points closest to the fault ($x=\pm0.5$km). The surface creep rate is estimated by differencing the modeled fault-parallel velocities across the fault. Example diagrams of surface creep rate estimation for selected profiles are shown in Figure 5. The standard deviation of the estimated creep rate is obtained via error propagation in this procedure.

The InSAR-derived surface creep-rate distribution is variable along the fault (Figure 6b) and matches the fault crossing baseline surveys from Zhang et al. (2018) at their site locations. To first order, the distribution of surface creep rate also appears correlated with nearby recent ruptures: 1) average creep rates of ~2.5 mm/yr near the 1981 Daofu earthquake rupture and 2) surface creep of up to ~5 mm/yr around the 2014 Kangding earthquake rupture, indicating that the surface creep is possibly linked to afterslip from these seismic events. In Section 3.4, we will investigate the SE segment of the XSF in more detail, given the coverage of Sentinel-1 data starting just before and continuing after the 2014 Kangding earthquake.

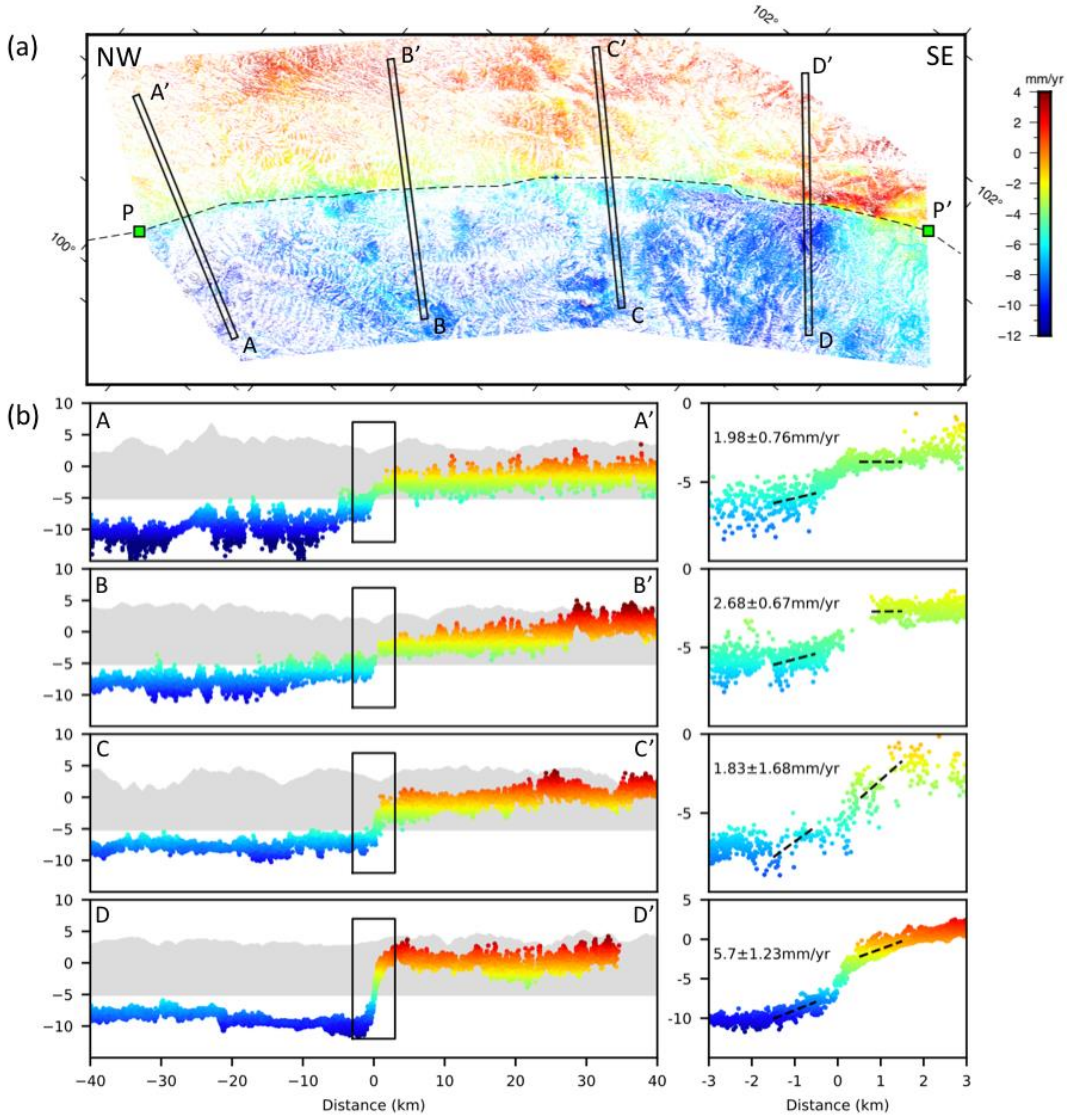

Figure 5. (a) Close-up view of the fault-parallel velocity field in Figure 4(c). Green squares on fault are same as those shown in Fig. 3c. (b) Fault-perpendicular velocity profiles (AA', BB', CC' and DD') with their locations shown in (a). Gray shaded areas represent the topography along the corresponding profiles. Right panels show the near-fault zoom of the left panels. The linear fit of the velocity trends at each side of the fault (0.5-1.5km) are labeled in dashed lines. The estimated surface creep rates are labeled in each profile.

3.3 Coupling model along the XSF inverted from 2014-2019 deformation

To capture the subsurface slip distribution along the XSF using InSAR data from both the near and far field, we conduct a two-step inversion following Chaussard et al. (2015). While it is likely that the deep slip rate and locking depth change along fault strike, there is also some trade-off between the locking depth and deep slip rate, where higher slip rates are obtained when using deeper locking depths. Therefore, here we assume a constant locking depth of 12 km and only solve for a uniform deep slip rate along the XSF. We first invert for the long-term slip rate using

a 1000-km-wide (effectively semi-infinite) vertical deep extension of the surface fault trace below 12 km. We also extend the deep model dislocation far beyond the lateral edges of our model domain to prevent spurious far-field deformation gradients associated with the fault terminations. The geometry of the deep dislocation model is shown in Figure S5. The InSAR LOS velocities (Figure 4 a, b) are downsampled for denser sampling near fault and a sparser grid away from the fault trace. Pixels within one locking depth away from the fault trace are masked out given that the near field data may include contributions from shallow creep. The inverted deep slip rate is 12.11 mm/yr with RMS residuals of 0.68 mm/yr. The resampled observed, modeled and residual long-wavelength LOS velocities for ascending and descending tracks are shown in Figure S6, while Figure S8 shows the full-resolution results. The predicted GPS velocities using our derived deep dislocation model match the GPS observations as well (RMS_{GPS} 2.04 mm/yr, Figure S7). We also tested the inversion results for different locking depths, where 10 km locking depth would lead to a deep slip rate of 11.24 mm/yr (RMS_{SAR} 0.68 mm/yr, RMS_{GPS} 2.09 mm/yr) and 14 km would lead to 12.99 mm/yr (RMS_{SAR} 0.69 mm/yr, RMS_{GPS} 1.99 mm/yr).

For the inversion of shallow fault creep, we use the residual velocity maps from the deep dislocation model (Figure S8 c, f). We downsample the InSAR data iteratively using a quadtree algorithm (Simons et al., 2002; Wang & Fialko, 2015) to ensure more data points in areas with high velocity gradients near the fault trace. Pixels within 0.5 km of the fault trace are masked out to avoid averaging across the fault and smearing out the sharp velocity gradient through downsampling. We assume a vertical fault geometry due to the lack of evidence of variations in the along-strike fault dip. The model fault is 20 km wide, allowed to extend below the 12 km locking depth to accommodate potential deep afterslip of the 2014 Kangding earthquake. We discretized the fault into 1×1 km patches at the surface, and the patch size increases with depth to compensate for the loss of resolution (Fialko, 2004). We choose the smoothing parameter ($\boldsymbol{\lambda}$ in Eq 1) to be 0.01, relying on the trade-off curve between the smoothing parameter and RMS of the residuals shown in Figure S9. In the shallow slip inversion, we only allow left-lateral strike slip and fix the dip-slip component to zero.

The preferred coupling model is shown in Figure 6d and corresponding distributed creep-rate model in Figure 7. The observed and modeled LOS velocity maps are shown in Figure 8, with an RMS of 0.70 mm/yr. In the model, patches with slip rate lower than 1.40 mm/yr are colored in white and are considered to be locked (Figure 7). The XSF represents a partially coupled fault with asperities, and we identify several areas with shallow creep of up to ~4-15 mm/yr (e.g., patches near Xialatuo site, Goupu site, etc). The high slip rates exceeding the tectonic loading rate on the SE part of the fault is likely associated with postseismic processes of the 2014 Kangding earthquake. If we assume a 12.11 mm/yr long-term slip rate and a locking depth of 12 km, 26% of the interseismic strain is released through aseismic slip along this 270-km-long section of the XSF, during the time period of December 2014 to July 2019. The percentage of the moment budget being released will be higher for a lower long-term slip rate and/or a shallower locking depth.

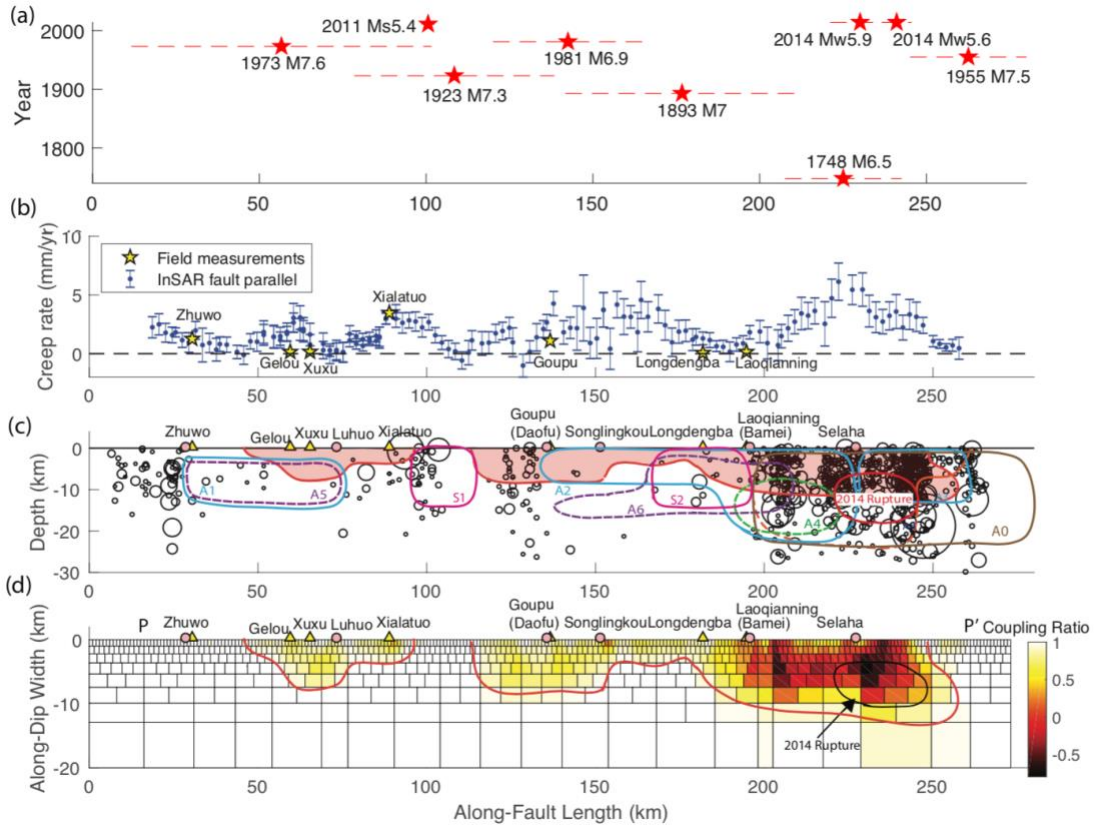

Figure 6. (a) Spatio-temporal distribution of the most recent historical earthquake ruptures along the XSF. (b) Creep rate variation along the XSF estimated from fault-perpendicular velocity profiles. The averaged surface creep-rate measurements (1970s-2010s) from Zhang et al. (2018) are shown with yellow stars. (c) Cross-section of microseismicity and comparisons of identified asperities along the XSF. Black circles show M≥1.5 seismicity within 10 km of the XSF from China Seismic Experiment (2009-2019; Wu et al., 2019). A0: seismicity gap identified by Wen et al. (2008). A1-A3: asperities suggested by Jiang et al. (2015). A4: asperity proposed by Yi et al. (2005). A5-A6: asperities from Zhang et al. (2018). S1-S2: potential locked asperities identified by this study. (d) 2D view of the fault coupling distribution between 2014.12-2019.7 with outlined shallow creeping area. The coupling ratio is defined to be one when the fault is fully locked and zero when it is slipping at a tectonic loading rate of 12.11 mm/yr. Negative values indicate creep rates in excess of long-term values.

316

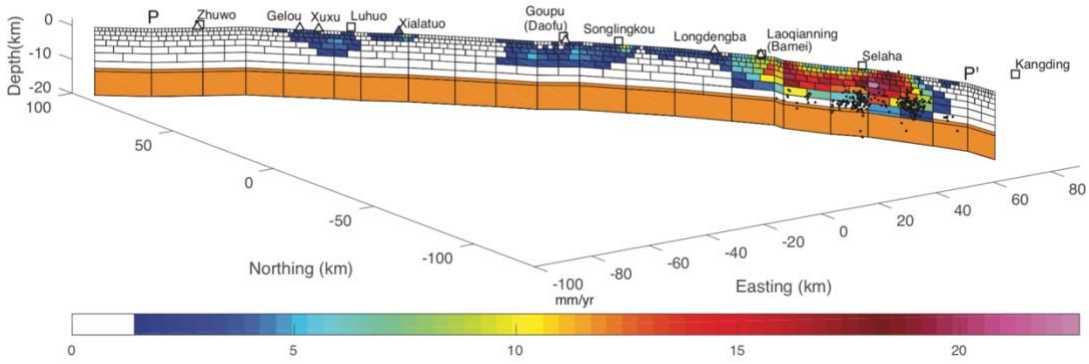

317
318

319 **Figure 7**. The inverted interseismic shallow slip model using the average velocity map between
320 2014.12-2019.7 in the Xianshuihe Region. The model also includes 1000-km-wide deep
321 dislocations below 12 km slipping at 12.11 mm/yr with lateral extensions that go far beyond the
322 fault tips to account for the long-wavelength interseismic strain accumulation (see Figure S5). The
323 locations of P and P' are marked in Figure 4. Fault crossing baselines from Zhang et al. (2018) are
324 shown as triangles colored by the reported along-strike slip rates. Locations of major cities along
325 the XSF are labeled with squares.
326

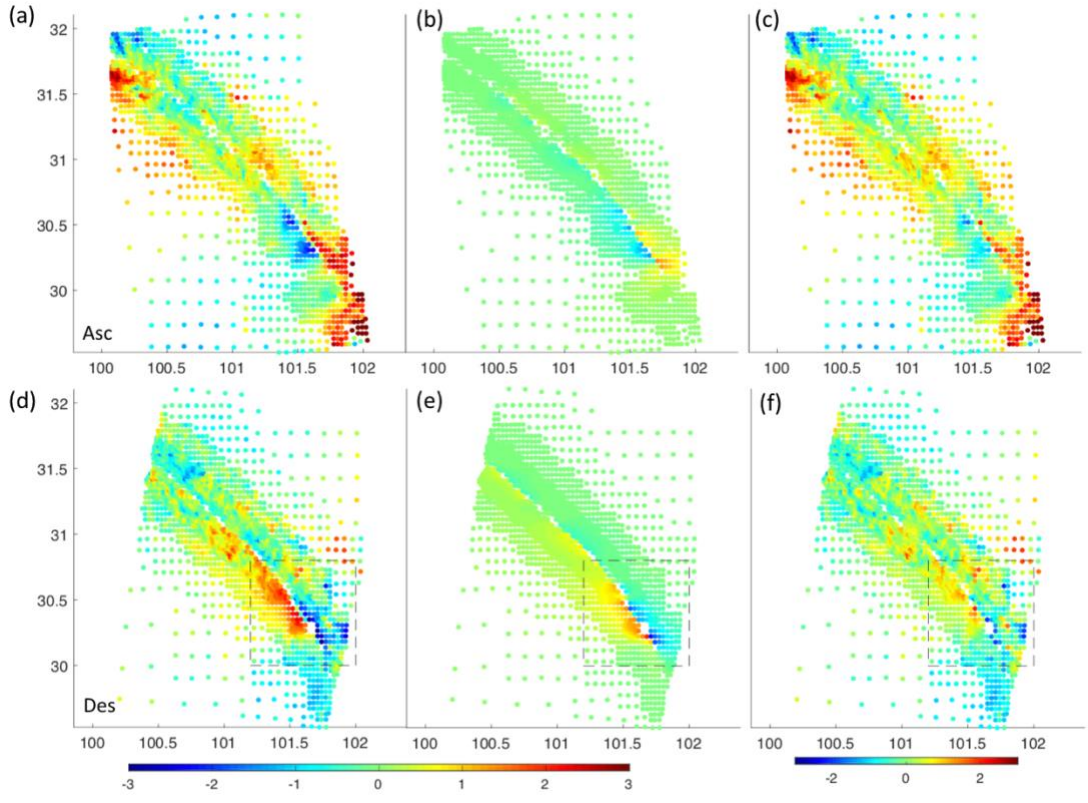

327

328 **Figure 8.** Comparison of downsampled observed and modeled short-wavelength LOS velocities
329 from both ascending and descending Sentinel-1 geometries. (a-c) are observed, modeled, and

observed-minus-modeled residuals for ascending track 26. (d-f) are corresponding maps for descending orbit 135. Descending LOS velocities inside the black dashed box are used in the Kangding afterslip study, a zoom-in map of the sub-region is shown in Figure S14. Note that in (a) and (d), we have already subtracted the velocity field due 12.11 mm/yr of slip on a buried dislocation below 12 km.

3.4 The 2014 Kangding earthquake sequence and its coseismic slip model

Unlike the rather simple central segment, the southeastern part of the Xianshuihe Fault zone is more complex, where the fault splits into three branches, the Yalahe fault, the Selaha fault and the Zheduotang fault (Fang et al., 2015; Bai et al., 2018). The November 22, 2014 M_w5.9 Kangding earthquake was the most recent moderate earthquake along the XSF. The earthquake triggered more than 1000 aftershocks, including a M_w5.6 earthquake on November 25, 2014 (Jiang et al., 2015a). No surface ruptures were found in field investigations following the two events (Jiang et al., 2015a). The M_w5.9 event was inferred to have occurred on the Selaha branch, whereas the M_w5.6 event likely occurred on the northern extension of the Zheduotang branch of the XSF (Jiang et al., 2015a).

We use the relocated aftershocks from Fang et al. (2015) to determine the fault geometry of the coseismic slip model. The aftershocks are divided into two clusters representing aftershocks of the M_w5.9 and M_w5.6 event, respectively. Based on the spatial extent of the aftershocks, we set the fault lengths to be 20 km and 10 km for the two events and their downdip widths to 20 km. For each aftershock cluster, we use the principal component analysis (PCA) to find the fault strike that minimizes the residuals of the distances between the aftershock locations and the fault plane. The optimal strikes of the M_w5.9 and M_w5.6 fault planes are 140.95° and 152.98°, respectively. As the dips derived from PCA are near vertical (89.34° and 84.35°) and the aftershocks are quite scattered at depth, we did not use the inverted dip angles from the PCA. For the smaller M_w5.6 event, we assume the fault to be vertical. For the M_w5.9 event, the fault location was originally determined by the aftershocks assuming a vertical fault plane. We then added the fault dip and eastward shift of the surface fault trace location as a free parameter to account for the location ambiguity. We found a dip angle of 80° to the southwest and a 1500 m eastward shift that minimize the RMS residual from the grid search analysis for the M_w5.9 fault plane (Figure S10). After this adjustment, the fault centers for the M_w5.9 and M_w5.6 events are (101.66°, 30.30°) and (101.72°, 30.19°), respectively.

Next, we solve for the distributed coseismic slip on the two fault planes using the downsampled ascending and descending interferograms. Our preferred model is shown in Figure 9, where the coseismic slip concentrates between 8-12 km depth with a maximum slip of about 0.8 m. The slip diminishes to near zero at ~5km depth and no slip was found in the shallowest 3-4 km, representing a blind rupture model with a substantial shallow slip deficit. The geodetic derived seismic moment is M_w6.15, which is far more than the M_w5.9 moment magnitude derived from the seismic data (M_w5.99 including all aftershocks). Previously published slip models also documented a similar discrepancy, where Jiang et al. (2015a) found the geodetic derived seismic moment magnitude to be M_w6.2 from ALOS-2 data. Xie et al. (2017) discuss the possible factors that could lead to such discrepancies, such as the choice of regional shear modulus, the inclusion of early afterslip in the coseismic interferograms, and various assumptions made in either estimate. In section 4.3, a stress-driven afterslip forward model is used to address the possible contribution of early afterslip during

the 14 and 21 days between the mainshock and acquisitions of the post-event ascending and descending image, respectively.

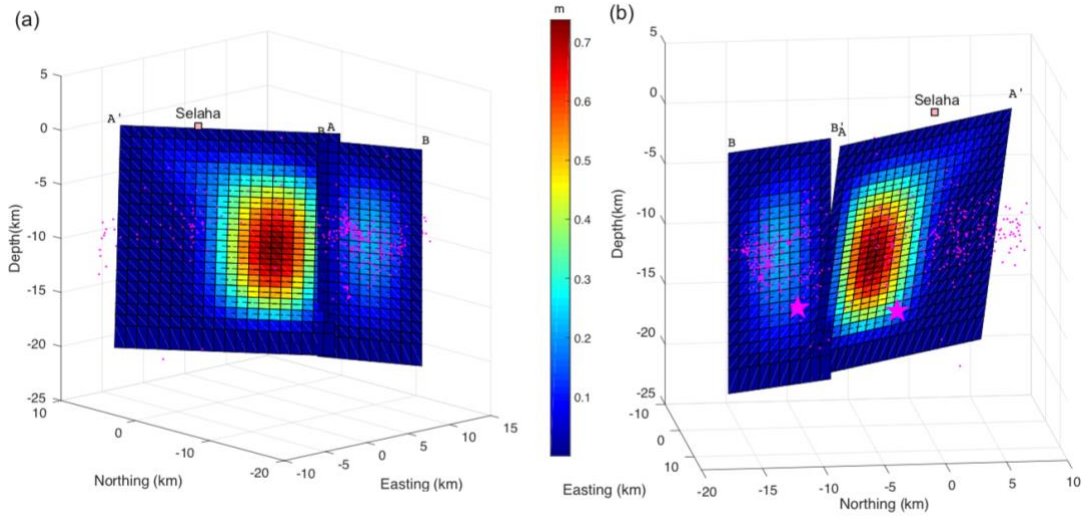

Figure 9. The best-fitting coseismic slip model of the Kangding earthquake. (a) and (b) show the slip model from opposite viewing geometries. Magenta dots show the first 24 days of relocated aftershocks of the 2014 Kangding earthquake sequence (Fang et al., 2015). We use 0.008 as our preferred smoothing parameter in the inversion.

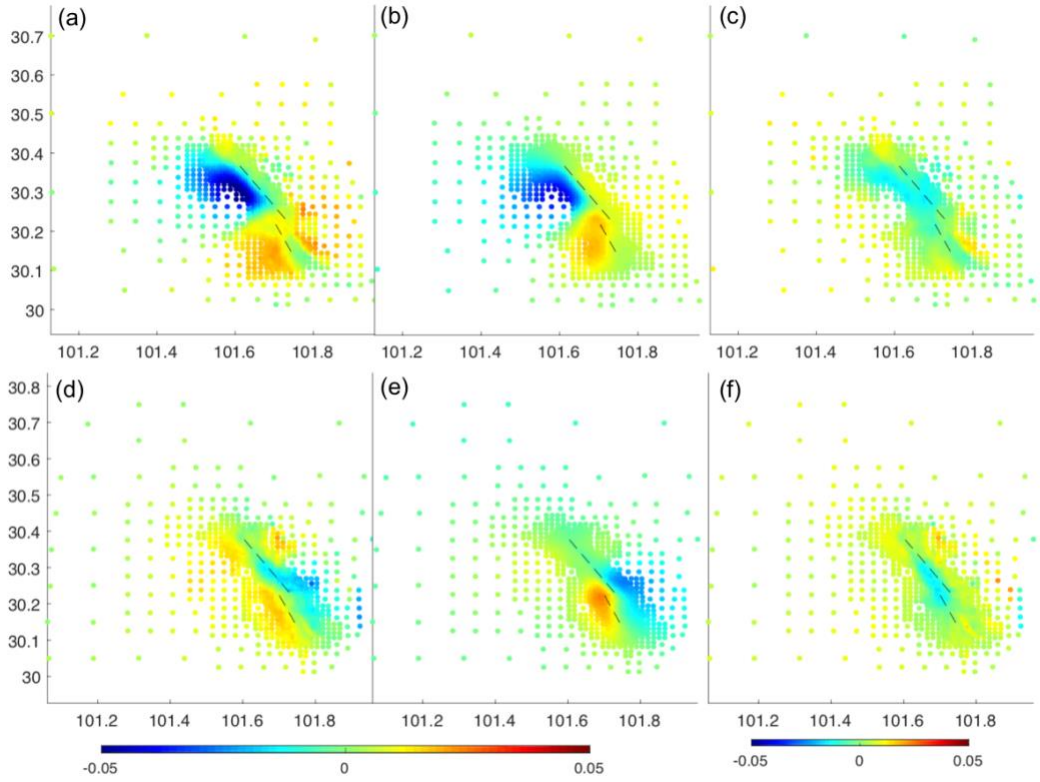

Figure 10. Comparison of observed and modeled coseismic deformation of Kangding earthquake from both ascending and descending Sentinel-1 geometries. (a-c) are the downsampled observed, modeled, and observed-minus-modeled residuals for ascending track 26. (d-f) are corresponding

maps for descending orbit 135. Black dashed lines indicate surface traces of the fault rupture model in Figure 9.

3.5 Temporal characteristics of the postseismic deformation in the Kangding region

After the removal of deformation from the deep interseismic dislocation model, the largest fault offsets are observed along the southeast section of the XSF (Figure 8), near the rupture of the 2014 Kangding earthquake sequence. A corresponding pattern of high slip rates is also found in the inverted creep-rate model (Figure 7) and patches with inferred negative coupling (excess slip) in the coupling model (Figure 6d). The modeled fault slip rate of up to 22 mm/yr in the Kangding region exceeds the interseismic loading rate (~12 mm/yr). Considering the InSAR data spans the postseismic period of the 2014 Kangding earthquake sequence, such high slip is probably related to postseismic afterslip. Given the Kangding earthquake did not rupture to the surface and its coseismic slip model shows a clear shallow slip deficit (Figure 9), we infer that the earthquake ruptured a locked asperity at depth and the rapid creep represents afterslip in the shallow portions of the fault up dip of the rupture.

Therefore, a timeseries analysis is carried out using 189 additional interferograms from track 135 to assess the time dependence of the afterslip (data described in section 2.1). The LOS velocity map from the timeseries analysis (Figure 11a) is noisier but otherwise comparable to that formed from the manually selected interferograms (Figure 4b). Given the limited signal to noise ratio of the cumulative displacements solved by SBAS, we take three pairs of 1~2-km-wide and ~15-km-long swaths on each side of the fault and focus on the average cross-fault timeseries differences between each pair of swaths. Multiple timeseries differences are taken from subswaths ranging from 0-1 km, 1-2 km, 1-3km, and 3-5 km away from the fault trace on each side of the fault.

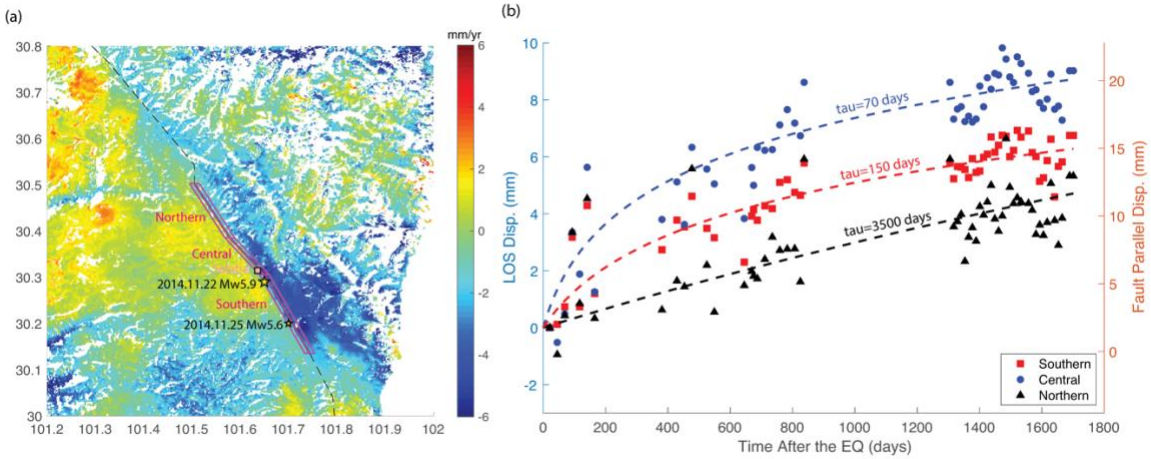

Figure 11. (a) Average LOS velocity map of the SE section of the XSF for descending track 135 derived from the timeseries analysis (December 2014-July 2019). Red color represents radar range increase and blue color represents range decrease. Epicenters of the 2014 Kangding earthquake and its largest aftershock are labeled and shown as yellow stars. The inferred fault geometry in this region is shown by the dashed line. Magenta boxes outline the near-fault patches that are used for differencing cross-fault time series for the northern, central and southern Kangding fault sections, respectively. (b) Averaged cross-fault time series of the cumulative LOS displacement differences along the northern, central, and southern fault sections shown in (a). Dashed lines show the fitting

curves on each fault sections assuming a logarithmic afterslip decay time with characteristic decay times labeled on the curve. Blue y-axis shows the LOS displacements whereas the orange axis on the right shows the corresponding fault parallel displacement assuming all motions are fault parallel.

The averaged cumulative LOS displacement differences across the fault at 0-1km in the northern, central and southern swaths are shown in Figure 11b. For reference, the stacked averaged timeseries of patches west and east of the fault prior to differencing are shown in Figure S11. The cumulative displacement shows a temporal decay and can be fitted with a logarithmic function, consistent with the assumption that the deformation is associated with transient creep or afterslip (e.g. Savage & Svarc, 2009; Savage et al., 2005). Therefore, we fit the timeseries using Eq 3, where $c1$ and $c2$ are constants, t is the days after the earthquake, and τ is the characteristic decay time. We first fit the timeseries for each swath separately and find the characteristic decay times τ that minimize the RMS misfit for the northern, central and southern swath to be 3500 days, 70 days and 150 days, respectively (Figure 11b, Figure S12). We repeated the process and found the best-fitting characteristic decay times for all swath pairs at distances further away from the fault (Table S2). The northern swath has a distinctly longer characteristic decay time than the other two swaths and the linear model fits equally well compared with the log-decay model. This indicates the slip in the northern swath is less likely to be afterslip. The characteristic decay time reduced from 3500 days to 1500 days for swath pairs further away from the fault, indicating some decaying slip at depth, regardless of it having small contribution overall. As for the central and southern swaths, the characteristic decay times are the shortest near the fault trace (70 and 150 days at 0-1 km) and become longer (500 and 1000 days at 3-5 km) when moving away from the fault trace. Such a pattern could possibly be due to a shallow decaying afterslip. As the resolved characteristic decay time changes with distance from the fault, we select $\tau = 250$ days as the characteristic decay time for the whole section in the afterslip analysis as an approximation, which is the characteristic decay time for the central and southern segment at 1-3 km swaths.

$$\mathrm{disp(t)} = c1 + c2 \log\left(1 + \frac{t}{\tau}\right) \qquad \text{(Eq 3)}$$

$$\Delta\mathrm{disp(t1,t2)} = \mathrm{disp(t1)} - \mathrm{disp(t2)} = c2\left[\log\left(1 + \frac{t1}{\tau}\right) - \log\left(1 + \frac{t2}{\tau}\right)\right] \qquad \text{(Eq 4)}$$

$$S = \sum \frac{\Delta\mathrm{disp(t1,t2)}}{\Delta\mathrm{disp(0,tmax)}} \qquad \text{(Eq 5)}$$

Based on this relationship and assuming $\tau = 250$ days, only 2.7% and 4.0% of the postseismic moment is released in the first 14 and 21 days. Thus, the ascending and descending coseismic interferogram spanning 14 and 21 days after the earthquake will include 2.7% and 4.0% of the afterslip deformation. For reference, the moment release would be 1.2% and 1.9% if we assume $\tau = 1500$ days, and 5.7% and 8.2% if we assume 70 days.

Using the relationship in Eq 3, we can reconstruct the cumulative displacement map from the average velocity map for the Kangding section of the XSF that will be further discussed in Section 4.3. For each interferogram, the displacement in the corresponding time span can be calculated using Eq 4. When $t2 = \mathrm{tmax}$ (end of the observation period) and $t1 = 0$, the displacement corresponds to the total cumulative postseismic displacement. Combined with the weight of each

time span in the formation of the average velocity map (Figure S13), a cumulative displacement map can be reconstructed by applying a scaling factor $\boldsymbol{S}$ to the average velocity map obtained through stacking (Eq 5, Figure S14). The scaling factor is $\boldsymbol{S}$=5.09 when $\tau = 250$. If we assume a steady-slip scenario, $\boldsymbol{S}$=4.49 and is equivalent to the total time span (in years) used in the stacking. Note that we did not use the cumulative displacement derived from SBAS given its high uncertainties introduced by the low signal and high atmospheric noise levels. Therefore, the spatial pattern of the reconstructed deformation is the same as the average velocity map. We also ignore the possible contribution of other postseismic mechanisms such as viscoelastic relaxation and poroelastic rebound. The reconstructed cumulative displacement map relies on the assumption of a spatially uniform logarithmic decay of the signal.

4 Discussion

4.1 Implications and limitations of the interseismic velocity map and coupling model

We have to admit that the substantial vegetation cover, the high atmospheric noise content and the relatively low tectonic signal (~12 mm/yr) along the XSF make the extraction of the interseismic deformation signal challenging. In this study, we use InSAR data spanning December 2014 to August 2019 to form interseismic average velocity maps from a selected subset of high-quality interferograms that show a clear offset along the fault and have relatively modest atmospheric artifacts. The signal-to-noise ratio in a single interferogram spanning a year or longer can be significantly improved since the long-term interferogram will capture more deformation assuming the same noise level (Figure 2). Therefore, we obtained a regional high-resolution interseismic velocity field in the XSF region by using manually selected long-term interferograms. However, we acknowledge the existence of remaining atmospheric noise in the stacked average velocity maps, as is evident in both the observations (Figure 4) and the residual maps for the coupling model (Figure 8). As we use the averaged velocity maps for the coupling model inversion, this model does not address temporal variation of the deformation field and slip distribution. The interferograms are unevenly distributed in time, and the weight of each time period in the mean rate estimate is unbalanced (Figure S13). Such unbalanced sampling in time will not affect our coupling model if the slip behavior along the fault is temporally invariant. We were not able to extract the temporal evolution of the slip behavior due to data limitations, except for the SE section of the XSF near the 2014 Kangding earthquake rupture, where a decaying pattern is captured. Hence, we chose to keep the steady slip-rate assumption and use the averaged velocity map to derive the coupling model, regardless of the potential underestimation of slip rate in the SE section (~12%).

Due to the inherent limitations of the SAR observations, multiple constraints were added when inverting for our preferred coupling model. We first masked the near field data, fix the locking depth at 12 km and inverted for the long-term deep dislocation slip rate. We do not allow the slip rate and locking depth to vary along strike, despite of geologic studies reporting a decrease in slip rate along the XSF from 10-15 mm/yr in the northwest to 5-10 mm/yr in the southeast (e.g. Allen et al., 1991; Xu et al., 2003). While this model comes with a number of inherent uncertainties, the inferred coupling distribution can provide valuable observational constraints of variable fault behavior along the XSF. Previous models focused on the coupling status and strain accumulation along sections of the XSF (e.g. Jiang et al., 2015b, Li et al., 2018). However, those studies mainly

depend on GPS to constrain their analysis and do not have sufficient spatial resolution. Our up-to-date, high-resolution geodetic observations provide additional data constraints that should be of value for future investigations of the XSF.

4.2 Implications for the seismic potential on the XSF

The XSF is one of the most seismically active regions in China. Being one of the major faults that accommodates the partitioning of regional deformation at the eastern boundary of the Tibetan Plateau (Fig. 1), all segments of the XSF appear to have ruptured several times since 1700. Wen et al. (2008) investigated the modern and historical records of the seismic intensity, rupture extent and geological investigations, and compiled a detailed rupture history along the XSF. Recent ruptures since 1893 are shown in Figure 6a. The spatiotemporal pattern of historical ruptures along the XSF does not seem characteristic, that is, the fault slip appears to be neither slip nor time predictable. However, the historical rupture records on a fault segment are still valuable as one can calculate the slip deficit since the latest earthquake and infer the seismic potential on the fault assuming all accumulated seismic moment will be released by future seismic events. In this section, we estimate the equivalent seismic moment deficit along corresponding fault segments based on a locking depth of 12 km and deep slip rate of 12.11 mm/yr, consistent with the values used for deriving our coupling model (Figure 7). If the slip rate is decreased to 10 mm/yr, the estimated cumulative moment deficit will decrease by ~M_w0.05. Likewise, if the locking depth is increased to 14 km, the estimated equivalent cumulative seismic moment will rise by ~M_w0.05.

A seismic gap was identified along a fault segment between the Bamei and Kangding area (A0 in Figure 6c), where the most recent event (M ~6.75) occurred in 1748 (Wen et al., 2008). The 2014 Kangding earthquake sequence occurred within this proposed seismic gap. However, the spatial extent of the rupture and the total seismic moment release (M_w5.99 including aftershocks) does not compensate for the slip deficit that has accumulated since 1748 (corresponding to M_w>7.25). The moment release of the 2014 Kangding earthquake sequence only equals ~10 years of strain accumulation on the estimated 1748 rupture asperity, less than 4% of the total. In addition to the A0 seismic gap, we note two segments along the XSF that have not ruptured for about a century. One of them is a ~20-km-long segment SE of the Xialatuo area (S1 in Figure 6c), where the latest recorded rupture was a M 7.3 event in 1923. No surface creep is identified on that segment, indicating the fault segment is probably a fully locked asperity and accumulating strain interseismically. The slip deficit on segment S1 since 1923 is capable of generating a M_w6.55. The second identified segment with high seismic potential is located between NW of Longdengba and Laoqianning/Bamei (S2 in Figure 6c). The latest rupture on the corresponding segment S2 occurred in 1893 and the cumulative slip deficit since that M ~7 event is capable of generating a M_w6.74 event. If we combine the surrounding areas with substantial slip deficit accumulated since their latest rupture from Longdengba to Kangding (A0+S2), the combined segment has a seismic potential of up to ~M_w7.29.

Our work further addresses the locking status and seismic potential on the fault by adding evidence from geodetic observations and quantitative estimates of moment released by aseismic fault slip. From the coupling model derived from InSAR observations (Figure 6,7), we mapped the detailed distribution of the shallow creeping sections of the fault (Figure 6c), where a total of 26% of the interseismic strain is released through aseismic slip during the observation period. If the slip rate is decreased to 10 mm/yr or the locking depth changed to 10 km, ~30% of the interseismic strain

will be released through aseismic slip. Moreover, if we assume all creeping patches do not contribute to interseismic strain accumulation and their slip budget is fully accommodated by aseismic slip, including both steady creep and afterslip following nearby ruptures, there will be a ~40% reduction of seismic potential.

In addition to the historical earthquake records that document the longer-term seismic slip history along the XSF, modern microseismicity provides additional evidence of the locking status along the fault. Yi et al. (2005) consider the spatial distribution of b-values and propose a probable asperity between Bamei and Selaha (A4 in Figure 6c) due to its unusually low b-value (0.66-0.73). Zhang et al. (2018) also identified a locked asperity between Zhuwo and Luhuo (A5) and another one between Goupu/Daofu and Laoqianning (A6), evidenced by the sparsity of microseismicity on the fault along these sections in the past decade. The asperity locations derived from microseismicity are generally consistent with our aseismic slip model, where the proposed locked patches are also free of or have limited shallow aseismic slip.

The primary discrepancy occurs on the segment between Bamei and Selaha, the northern extension of the 2014 Kangding earthquake rupture (hereinafter referred to as N-Selaha segment), where we find substantial aseismic slip and the segment appears fully uncoupled (Figure 6d and 7) in our model. In contrast, the N-Selaha segment has been identified as a potential asperity by Yi et al. (2005) because of low b-values as well as by Jiang et al. (2015b) from their joint inversion of InSAR and GPS data using a viscoelastic model. This could indicate that the coupling status on the N-Selaha segment changed from locked to fully uncoupled after the 2014 Kangding earthquake. One interpretation for this could be that after the 2014 Kangding earthquake ruptured the locked asperity, and slip on this segment occurred post-seismically. In summary, though the Kangding earthquake and its afterslip released part of the accumulated strain on a previously identified "seismic gap", the remaining slip deficit is still capable of generating a ~M7 event. Enhanced seismic and geodetic monitoring will be crucial to further improve the seismic hazard evaluation and quantification of earthquake potential along the XSF.

4.3 Possible mechanisms of the substantial afterslip in the Kangding region

Substantial near fault deformation is observed near the 2014 Kangding earthquake rupture since the event. The inverted fault slip on the corresponding fault patches far exceeds the tectonic loading rate and the temporal evolution of the deformation can be characterized by a logarithmic decay function, indicating that such deformation is probably due to postseismic afterslip. One common explanation for the origin of afterslip is that it is directly driven by the coseismic stress change (Bürgmann, 2018). To test if the kinematically inverted slip model makes physical sense, we use a stress-driven forward model to simulate the possible afterslip induced by the coseismic stress changes.

The stress-driven afterslip modeling is conducted using Unicycle (Barbot, 2018; Barbot et al., 2017). We assume a steady-state, rate-strengthening friction law without healing and slip weakening effects. In this simplification, the slip evolution can be represented by Eq 6 (Barbot et al., 2009; Wang & Bürgmann, 2020). All fault patches are set to be velocity strengthening except for the coseismic rupture area, where patches with negative stress change are pinned and not allowed to slip. As the temporal evolution of the slip behavior is not well constrained, we do not seek to find the best-fitting frictional properties of the fault interface, that is, the exact values of

585 $\mathbf{a\sigma}$ and V_0 are not discussed. We only focus on the slip value at full relaxation, which indicates the
586 maximum possible afterslip that could be induced by the coseismic rupture.

587 $$\mathbf{V = 2V_0 \sinh \frac{\Delta \tau}{a\sigma}} \qquad \text{(Eq 6)}$$

588 To simplify the simulation process, we use the fault geometry of the SE section of the coupling
589 model for the coseismic slip inversion, rather than using the best-fitting coseismic slip model with
590 two segments shown in Figure 9. The simplified slip model is shown in Figure S15 with the data
591 fitting shown in Figure S16. The same fault geometry is then used for the stress-driven afterslip
592 modeling, and the kinematic slip inversion and the stress-driven afterslip can be compared more
593 directly. We consider two kinematic slip models. The first kinematic model is taken from the
594 average slip rate in Figure 7 converted to cumulative slip by the scaling factor S=5.09, as described
595 in Section 3.5. For the second slip inversion, we do not allow afterslip to occur on patches with
596 negative coseismic stress change (same constraint as the stress-driven model). The inverted
597 kinematic slip models and simulated stress-driven afterslip model are shown in Figure 12, with the
598 modeled LOS displacements and their residuals. The deformation produced by the fully relaxed,
599 coseismic-stress-driven afterslip captures the observed cumulative deformation to first order, but
600 somewhat overpredicts the near-field deformation. The moment release from the afterslip is
601 equivalent to M_w5.91 for the kinematic inversion (Figure 12a), M_w5.88 for the constrained
602 kinematic inversion (Figure 12 b), and M_w6.03 (Figure 12 c) for the stress-driven forward model.
603 The maximum amplitude for the stress-driven model prediction is ~0.18 m, exceeding the
604 maximum slip in the kinematic model ~0.1m. However, if we apply the locked-asperity constraint
605 in the kinematic inversion, the maximum amplitude of the constrained kinematic model is about
606 the same as in the stress-driven model (Figure 12b). The misfits of the two kinematic inversions
607 are comparable, with RMS values of 2.59 mm and 2.63 mm. The fully-relaxed stress-driven model
608 has a higher misfit (RMS = 4.11 mm), which appears mainly due to a modest over-estimate of the
609 shallow afterslip and lack of slip further NW where significant displacements are observed (Figure
610 12c).

611 There is a substantial difference between the kinematic and stress-driven models NW of the
612 Kangding rupture along the N-Selaha and N-Bamei segments. The stress-driven afterslip model is
613 only capable of producing afterslip in the vicinity of the coseismic rupture and does not predict
614 slip along those segments located more than 20 km from the coseismic rupture (Figure 12c),
615 whereas the kinematic inversions suggest more than 0.1 m of slip in N-Selaha and N-Bamei (Figure
616 12a, b). That is, the inverted slip at depth along the N-Selaha and N-Bamei segments (Figure 12a)
617 cannot be explained by the coseismic stress change, and it also exceeds the long-term slip rate
618 (Figures 6d and 7). The excess deformation north of Selaha is quite clear from the residual map
619 (Figure 12c), and is unlikely to represent an artifact.

620

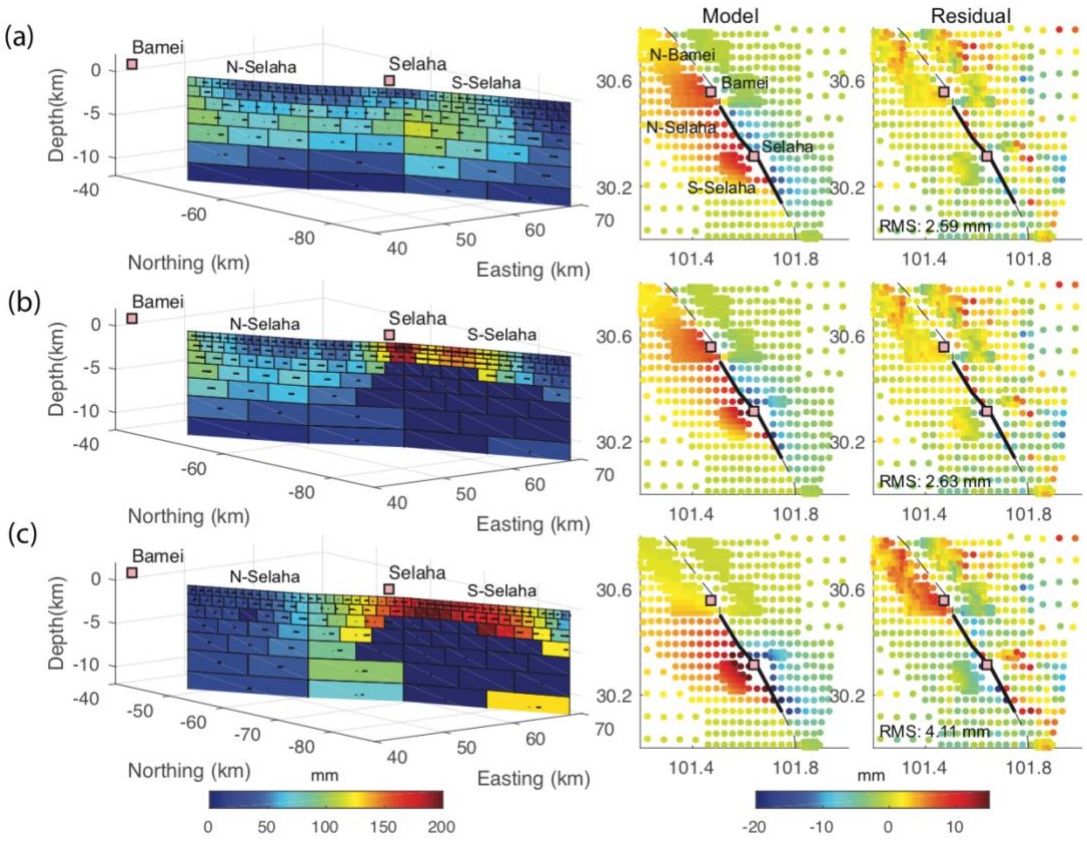

Figure 12. Cumulative 2014-2019 fault slip along the SE segment of the XSF derived from (a) kinematic inversion from Figure 7, (b) kinematic inversion imposing zero slip on patches that have coseismic slip >0.15m, and (c) coseismic-stress-driven afterslip model. Right panels show the modeled and observed-minus-modeled residual cumulative LOS displacements. RMS misfits for each afterslip model is labeled in the residual map.

Three possible explanations of the rapid aseismic slip beyond the immediate afterslip zone are discussed (Figure 12). One possibility is that the N-Selaha and N-Bamei segments exhibit steady creep interseismically and the observed shallow aseismic slip is independent of the earthquake (Figure 13a). This would be consistent with the near-linear evolution of the cross-fault LOS difference shown in Figure S12a, but not with the slip at depth apparently exceeding the long-term rate (Figures 6d, 7). Another scenario is that fault patches on those segments were originally velocity weakening and locked. The dynamic shaking of the 2014 Kangding earthquake may have perturbed the fault zone frictional properties and altered the corresponding patch from velocity weakening to velocity strengthening, allowing it to release ambient stress via aseismic slip (Figure 13b). The dynamic stress perturbation may have led to fault-zone compaction and associated pore pressure increase, thus temporally decreasing its fault strength. Finally, if the N-Selaha and N-Bamei segments of the XSF are only slightly velocity weakening at depth, the dynamic stress of

640 the earthquake could also trigger a slow slip event, though no clear pattern of acceleration or
641 deceleration is observed (Figure 13c).

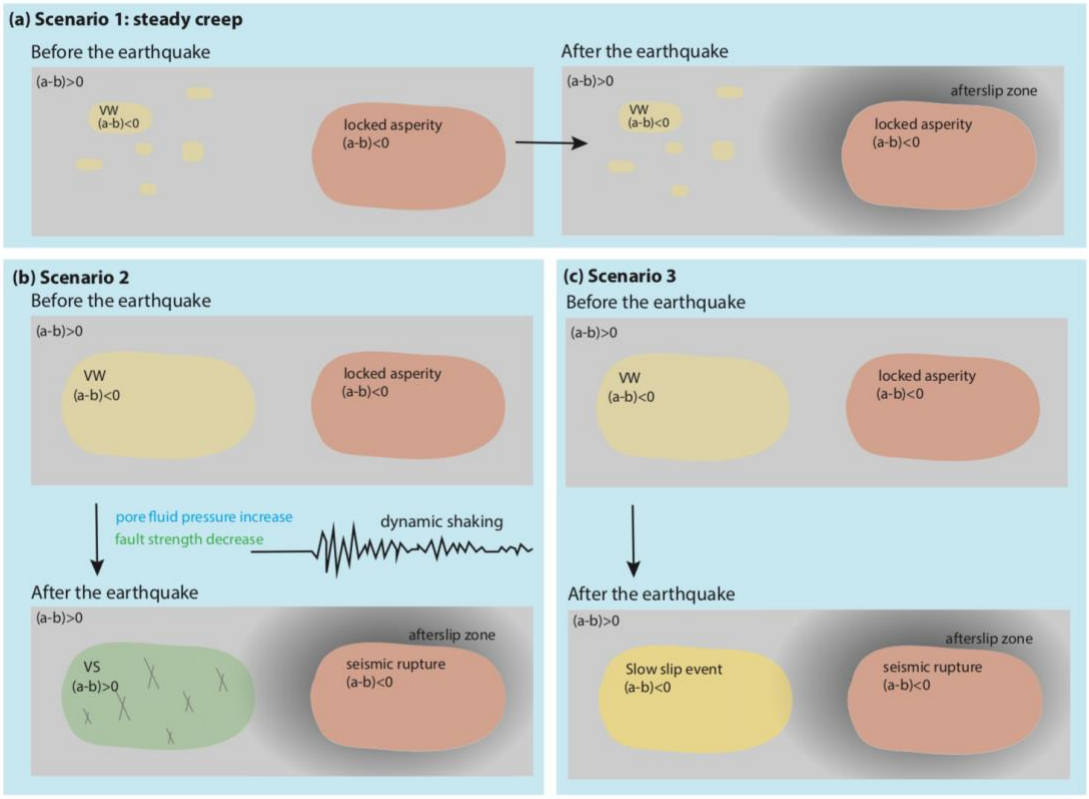

642

643 **Figure 13** Schematic plots for three possible explanations of the rapid aseismic slip north of the
644 rupture zone. (a) Scenario 1: steady creep independent of the seismic rupture. (b) Scenario 2:
645 dynamic shaking of the seismic waves altered the northern patch from velocity weakening to
646 velocity strengthening properties, allowing it to release ambient stress via aseismic slip. (c)
647 Scenario 3: enduring triggered slow slip event on modestly velocity weakening fault patch.

648

649 Slow slip events have been widely observed on continental strike-slip faults (e.g. Bilham, 1989;
650 Linde et al., 1996; Bokelmann & Kovach, 2003). More recent studies also observed slow slip
651 events triggered by nearby and remote earthquakes (e.g. Taira et al., 2014; Tymofyeyeva et al.,
652 2019). Using characteristically repeating earthquake activity to track slow slip, Taira et al. (2014)
653 observed substantial afterslip after the 1998 San Juan Bautista earthquake that cannot be explained
654 by the coseismic stress change, and attributed this to a triggered slow slip event. Moreover,
655 Tymofyeyeva et al. (2019) observed a slow slip event with the aid of InSAR and creepmeter data
656 on the southern San Andreas Fault that was remotely triggered by the distant 2018 M_w8.2 Chiapas,
657 Mexico earthquake. Detailed assessment of the temporal behavior of the slip evolution is crucial
658 for distinguishing such triggered slow slip events associated with shaking from earthquakes.

However, lacking near-field data to confirm the creep rate prior to the 2014 earthquake sequence, we cannot confirm or rule out either of the possible mechanisms.

5 Conclusions

We present a high-resolution interseismic velocity map along the XSF using ascending and descending Sentinel-1 InSAR data spanning from Dec 2014 to July 2019. The decomposed fault parallel velocity map reveals heterogeneous surface creep rates ranging from 0-6 mm/yr along the fault. We further derived distributed shallow slip and coupling models along the XSF. Several creeping patches are identified along the fault, including near Xialatuo, Goupu-Songlingkou and Bamei-Selaha-Kangding. The creeping sections release 26±4% of the interseismic moment budget during the observation period. Considering the most recent rupture history on each segment since 1748, we can identify two patches with high seismic potential 1) a ~20-km-long segment SE of the Xialatuo area, and 2) a section between NW of Longdengba and Laoqianning/Bamei. The former is capable of generating a M_w6.54 event since an M 7.3 event in 1923, whereas the latter is capable of generating a M_w6.73 event since an M 7 earthquake in 1893 and ~M_w7.28 if including surrounding locked areas. Along the SE section of the XSF, the inverted slip rate exceeds the tectonic loading rate. We performed a timeseries analysis of near-surface slip in the Kangding earthquake rupture region and the timeseries shows a logarithmic decay pattern of the cumulative displacement. The observed postseismic deformation along the rupture segment is consistent with the deformation produced by a coseismic-stress-driven afterslip model, indicating a velocity strengthening section of the fault up dip of the buried mainshock rupture. However, the shallow creep observed along the N-Selaha and N-Bamei segments is located outside of the coseismic static stress-change zone, suggesting this is a zone of rapid steady fault creep or represents the occurrence of an enduring triggered slow slip event.

Acknowledgments

The Sentinel-1 data were acquired from European Space Agency (ESA). Figures were generated by Generic Mapping Tools (GMT), MATLAB and Matplotlib. The regional seismic catalog was downloaded from the China Seismic Experiment Site (CSES, http://www.cses.ac.cn/) at http://124.17.4.85/?p=3792 (DOI:10.12093/01md.02.2019.05.v1). The work is supported by NASA Earth and Space Science and Technology (FINESST) program 80NSSC19K1330 and NASA Earth Surface and Interior Award NNX16AL17G.

References

Aagaard, B. T., Lienkaemper, J. J., & Schwartz, D. P. (2012). Probabilistic estimates of surface coseismic slip and afterslip for Hayward fault earthquakes. *Bulletin of the Seismological Society of America*. https://doi.org/10.1785/0120110200

Allen, C. R., Zhouli, L., Hong, Q., Xueze, W., Huawei, Z., & Weishi, H. (1991). Field study of a highly active fault zone : The Xianshuihe fault of southwestern China. *Geological Society of America Bulletin*.

Aslan, G., Lasserre, C., Cakir, Z., Ergintav, S., Özarpaci, S., Dogan, U., … Renard, F. (2019). Shallow Creep Along the 1999 Izmit Earthquake Rupture (Turkey) From GPS and High Temporal Resolution Interferometric Synthetic Aperture Radar Data (2011–2017). *Journal of Geophysical Research: Solid Earth*, *124*(2), 2218–2236. https://doi.org/10.1029/2018JB017022

Bai, M., Chevalier, M. L., Pan, J., Replumaz, A., Leloup, P. H., Métois, M., & Li, H. (2018). Southeastward increase of the late Quaternary slip-rate of the Xianshuihe fault, eastern Tibet. Geodynamic and seismic hazard implications. *Earth and Planetary Science Letters*, *485*, 19–31. https://doi.org/10.1016/j.epsl.2017.12.045

Barbot, S. (2018). Asthenosphere Flow Modulated by Megathrust Earthquake Cycles. *Geophysical Research Letters*. https://doi.org/10.1029/2018GL078197

Barbot, S., Fialko, Y., & Bock, Y. (2009). Postseismic deformation due to the Mw 6.0 2004 Parkfield earthquake: Stress-driven creep on a fault with spatially variable rate-and-state friction parameters. *Journal of Geophysical Research: Solid Earth*. https://doi.org/10.1029/2008JB005748

Barbot, S., Moore, J. D. P., & Lambert, V. (2017). Displacement and stress associated with distributed anelastic deformation in a half-space. *Bulletin of the Seismological Society of America*. https://doi.org/10.1785/0120160237

Berardino, P., Fornaro, G., Lanari, R., & Sansosti, E. (2002). A new algorithm for surface deformation monitoring based on small baseline differential SAR interferograms. *IEEE Transactions on Geoscience and Remote Sensing*. https://doi.org/10.1109/TGRS.2002.803792

Bilham, R. (1989). Surface slip subsequent to the 24 November 1987 Superstition Hills, California, earthquake monitored by digital creepmeters. *Bulletin - Seismological Society of America*.

Bokelmann, G. H. R., & Kovach, R. L. (2003). Long-term creep-rate changes and their causes. *Geophysical Research Letters*. https://doi.org/10.1029/2003GL017012

Bürgmann, R. (2018). The geophysics, geology and mechanics of slow fault slip. *Earth and Planetary Science Letters*. https://doi.org/10.1016/j.epsl.2018.04.062

Çakir, Z., Ergintav, S., Özener, H., Dogan, U., Akoglu, A. M., Meghraoui, M., & Reilinger, R. (2012). Onset of aseismic creep on major strike-slip faults. *Geology*. https://doi.org/10.1130/G33522.1

Chaussard, E., Bürgmann, R., Fattahi, H., Johnson, C. W., Nadeau, R., Taira, T., & Johanson, I. (2015). Interseismic coupling and refined earthquake potential on the Hayward-Calaveras fault zone. *Journal of Geophysical Research: Solid Earth*. https://doi.org/10.1002/2015JB012230

Chen, C. W., & Zebker, H. A. (2002). Phase unwrapping for large SAR interferograms:

735 Statistical segmentation and generalized network models. *IEEE Transactions on Geoscience*
736 *and Remote Sensing*. https://doi.org/10.1109/TGRS.2002.802453

737 Fang, L., Wu, J., Liu, J., Cheng, J., Jiang, C., Han, L., … Wu, Z. (2015). Preliminary report on
738 the 22 November 2014 Mw 6:1/Ms 6:3 Kangding Earthquake, Western Sichuan, China.
739 *Seismological Research Letters*. https://doi.org/10.1785/0220150006

740 Fialko, Y. (2004). Probing the mechanical properties of seismically active crust with space
741 geodesy : Study of the coseismic deformation due to the 1992 M w 7 . 3 Landers (southern
742 California) earthquake, *109*, 1–19. https://doi.org/10.1029/2003JB002756

743 Goldstein, R. M., & Werner, C. L. (1998). Radar interferogram filtering for geophysical
744 applications. *Geophysical Research Letters*. https://doi.org/10.1029/1998GL900033

745 Harris, R. A. (2017). Large earthquakes and creeping faults. *Reviews of Geophysics*.
746 https://doi.org/10.1002/2016RG000539

747 Jiang, G., Wen, Y., Liu, Y., Xu, X., Fang, L., Chen, G., … Xu, C. (2015a). Joint analysis of the
748 2014 Kangding, southwest China, earthquake sequence with seismicity relocation and
749 InSAR inversion. *Geophysical Research Letters*, *42*(9), 3273–3281.
750 https://doi.org/10.1002/2015GL063750

751 Jiang, G., Wen, Y., Liu, Y., Xu, X., Fang, L., Chen, G., … Xu, C. (2015b). Joint analysis of the
752 2014 Kangding, southwest China, earthquake sequence with seismicity relocation and
753 InSAR inversion. *Geophysical Research Letters*, *42*(9), 3273–3281.
754 https://doi.org/10.1002/2015GL063750

755 Jolivet, R., Lasserre, C., Doin, M. P., Guillaso, S., Peltzer, G., Dailu, R., … Xu, X. (2012).
756 Shallow creep on the Haiyuan fault (Gansu, China) revealed by SAR interferometry.
757 *Journal of Geophysical Research: Solid Earth*. https://doi.org/10.1029/2011JB008732

758 Khoshmanesh, M., Shirzaei, M., & Nadeau, R. M. (2015). Time-dependent model of aseismic
759 slip on the central San Andreas Fault from InSAR time series and repeating earthquakes.
760 *Journal of Geophysical Research: Solid Earth*. https://doi.org/10.1002/2015JB012039

761 Li, Y., Liu, M., Wang, Q., & Cui, D. (2018). Present-day crustal deformation and strain transfer
762 in northeastern Tibetan Plateau. *Earth and Planetary Science Letters*, *487*, 179–189.
763 https://doi.org/10.1016/j.epsl.2018.01.024

764 Liang, S., Gan, W., Shen, C., Xiao, G., Liu, J., Chen, W., … Zhou, D. (2013). Three-dimensional
765 velocity field of present-day crustal motion of the Tibetan Plateau derived from GPS
766 measurements. *Journal of Geophysical Research: Solid Earth*, *118*(10), 5722–5732.
767 https://doi.org/10.1002/2013JB010503

768 Linde, A. T., Gladwin, M. T., Johnston, M. J. S., Gwyther, R. L., & Bilham, R. G. (1996). A
769 slow earthquake sequence on the San Andreas fault. *Nature*.
770 https://doi.org/10.1038/383065a0

771 Sandwell, D., Mellors, R., Tong, X., Wei, M., & Wessel, P. (2011a). GMTSAR: An InSAR
772 Processing System Based on Generic Mapping Tools.

773 Sandwell, D., Mellors, R., Tong, X., Wei, M., & Wessel, P. (2011b). Open radar interferometry
774 software for mapping surface Deformation. *Eos, Transactions American Geophysical*
775 *Union*. https://doi.org/10.1029/2011eo280002

776 Savage, J. C., & Svarc, J. L. (2009). Postseismic relaxation following the 1992 M7.3 Landers
777 and 1999 M7.1 Hector Mine earthquakes, southern California. *Journal of Geophysical*
778 *Research: Solid Earth*. https://doi.org/10.1029/2008JB005938

779 Savage, J. C., Svarc, J. L., & Yu, S. B. (2005). Postseismic relaxation and transient creep.
780 *Journal of Geophysical Research: Solid Earth*. https://doi.org/10.1029/2005JB003687

781 Schmidt, D. A., & Bürgmann, R. (2003). Time-dependent land uplift and subsidence in the Santa
782 Clara valley, California, from a large interferometric synthetic aperture radar data set.
783 *Journal of Geophysical Research: Solid Earth*. https://doi.org/10.1029/2002jb002267

784 Shirzaei, M., & Bürgmann, R. (2013). Time-dependent model of creep on the Hayward fault
785 from joint inversion of 18 years of InSAR and surface creep data. *Journal of Geophysical*
786 *Research: Solid Earth*, *118*(4), 1733–1746. https://doi.org/10.1002/jgrb.50149

787 Simons, M., Fialko, Y., & Rivera, L. (2002). Coseismic deformation from the 1999 Mw 7.1
788 Hector Mine, California, earthquake as inferred from InSAR and GPS observations. *Bulletin*
789 *of the Seismological Society of America*. https://doi.org/10.1785/0120000933

790 Taira, T., Bürgmann, R., Nadeau, R. M., & Dreger, D. S. (2014). Variability of fault slip
791 behavior along the San Andreas Fault in the San Juan Bautista Region. *Journal of*
792 *Geophysical Research: Solid Earth*. https://doi.org/10.1002/2014JB011427

793 Tong, X., Sandwell, D. T., & Smith-Konter, B. (2013). High-resolution interseismic velocity
794 data along the San Andreas Fault from GPS and InSAR. *Journal of Geophysical Research:*
795 *Solid Earth*. https://doi.org/10.1029/2012JB009442

796 Tymofyeyeva, E., Fialko, Y., Jiang, J., Xu, X., Sandwell, D., Bilham, R., … Moafipoor, S.
797 (2019). Slow Slip Event On the Southern San Andreas Fault Triggered by the 2017 Mw8.2
798 Chiapas (Mexico) Earthquake. *Journal of Geophysical Research: Solid Earth*, *124*(9),
799 9956–9975. https://doi.org/10.1029/2018JB016765

800 Wang, H., Wright, T. J., & Biggs, J. (2009). Interseismic slip rate of the northwestern
801 Xianshuihe fault from InSAR data. *Geophysical Research Letters*, *36*(3), 1–5.
802 https://doi.org/10.1029/2008GL036560

803 Wang, K., & Bürgmann, R. (2020). Probing fault frictional properties during afterslip up- and
804 downdip of the 2017 Mw 7.3 Sarpol-e Zahab earthquake with space geodesy. *Journal of*
805 *Geophysical Research: Solid Earth*. https://doi.org/10.1029/2020jb020319

806 Wang, K., & Fialko, Y. (2015). Slip model of the 2015 Mw 7.8 Gorkha (Nepal) earthquake from

inversions of ALOS-2 and GPS data. *Geophysical Research Letters*. https://doi.org/10.1002/2015GL065201

Wei, M., Sandwell, D., & Fialko, Y. (2009). A silent Mw 4.7 slip event of October 2006 on the Superstition Hills fault, southern California. *Journal of Geophysical Research: Solid Earth*. https://doi.org/10.1029/2008JB006135

Wen, X. ze, Ma, S. li, Xu, X. wei, & He, Y. nian. (2008). Historical pattern and behavior of earthquake ruptures along the eastern boundary of the Sichuan-Yunnan faulted-block, southwestern China. *Physics of the Earth and Planetary Interiors*, *168*(1–2), 16–36. https://doi.org/10.1016/j.pepi.2008.04.013

Xie, Z., Zheng, Y., Liu, C., Shan, B., Riaz, M. S., & Xiong, X. (2017). An integrated analysis of source parameters, seismogenic structure, and seismic hazards related to the 2014 MS 6.3 Kangding earthquake, China. *Tectonophysics*. https://doi.org/10.1016/j.tecto.2017.04.030

Xu, X., Wen, X., Zheng, R., Ma, W., Song, F., & Yu, G. (2003). Pattern of latest tectonic motion and its dynamics for active blocks in Sichuan-Yunnan region, China. *Science in China, Series D: Earth Sciences*. https://doi.org/10.1360/03yd9020

Zhang, J., Wen, X. ze, Cao, J. ling, Yan, W., Yang, Y. lin, & Su, Q. (2018). Surface creep and slip-behavior segmentation along the northwestern Xianshuihe fault zone of southwestern China determined from decades of fault-crossing short-baseline and short-level surveys. *Tectonophysics*, *722*(July 2017), 356–372. https://doi.org/10.1016/j.tecto.2017.11.002

Zhang, L., Cao, D., Zhang, J., & Sui, L. (2019). Interseismic Fault Movement of Xianshuihe Fault Zone Based on Across-Fault Deformation Data and InSAR. *Pure and Applied Geophysics*, *176*(2), 649–667. https://doi.org/10.1007/s00024-018-1989-4

Zhang, P. Z. (2013). A review on active tectonics and deep crustal processes of the Western Sichuan region, eastern margin of the Tibetan Plateau. *Tectonophysics*. https://doi.org/10.1016/j.tecto.2012.02.021

Zheng, G., Wang, H., Wright, T. J., Lou, Y., Zhang, R., Zhang, W., … Wei, N. (2017). Crustal Deformation in the India-Eurasia Collision Zone From 25 Years of GPS Measurements. *Journal of Geophysical Research: Solid Earth*. https://doi.org/10.1002/2017JB014465

Cannot be added through Mendeley:

Jiang, G., Xu, X., Chen, G., Liu, Y., Fukahata, Y., Wang, H., ... & Xu, C. (2015b). Geodetic imaging of potential seismogenic asperities on the Xianshuihe-Anninghe-Zemuhe fault system, southwest China, with a new 3-D viscoelastic interseismic coupling model. *Journal of Geophysical Research: Solid Earth, 120(3), 1855-1873.*

Okada, Y. (1985). Surface deformation due to shear and tensile faults in a half-space. *Bulletin of the seismological society of America*, *75*(4), 1135-1154.

Wu, Z., X. Zhang, and K. Sun (2019), China Seismic Experiment Site: scientific challenges,

Acta Geologica Sinica - English Edition, 93(S1), 273-273, doi:10.1111/1755-6724.14084.

Xu, X. W., Han, Z. J., Yang, X. P., Zhang, S., Yu, G., Zhou, B., ... & Ran, Y. (2016). *Seismotectonic map in China and its adjacent regions.*

Yi, G.-X., J. Fang, and X.-Z. Wen (2005), Study on faulting behavior and fault segments for potential strong earthquake risk along the central southern segment of Xianshuihe fault zone based on current seismicity *(In Chinese)*, Earthquake, 25(1), 58–66.

Journal of Geophysical Research: Solid Earth

Supporting Information for

Partial coupling and earthquake potential along the Xianshuihe Fault, China

Yuexin Li[1] and Roland Bürgmann[1]

1 Department of Earth and Planetary Science and Berkeley Seismology Laboratory, University of California, Berkeley, CA, USA.

Contents of this file

Table S1 Selected interferograms used to form the average velocity maps

Tracks	Interferogram	Coherence	STD (radius)
T135	20141213_20161220	0.19	1.94
	20150106_20190121	0.13	3.21
	20150130_20190121	0.14	2.62
	20150412_20170308	0.13	2.63
	20150412_20181216	0.11	2.36
	20150506_20181029	0.12	2.01
	20150506_20181122	0.11	2.43
	20150506_20190226	0.11	2.63
	20150506_20190310	0.10	2.24
	20160921_20190521	0.12	4.46
	20161102_20181110	0.15	1.58
	20161220_20181228	0.15	1.82
	20170113_20181204	0.15	1.71
T33	20150111_20170325	0.12	1.59
	20150111_20171202	0.11	2.28
	20150111_20171214	0.11	2.22
	20150111_20181103	0.10	2.26
	20150111_20190102	0.10	2.75
	20150920_20180519	0.11	3.40
	20151201_20170325	0.14	1.46
	20151201_20171202	0.12	2.18
	20151201_20181221	0.10	3.33
	20151201_20190102	0.10	2.66
	20151201_20190126	0.10	2.01
	20160330_20180224	0.11	2.42
	20160610_20180519	0.12	2.21
	20161014_20181010	0.11	2.29
A26	20141206_20161231	0.17	3.72
	20141206_20170205	0.16	4.06
	20141206_20170217	0.15	4.47
	20141206_20180212	0.12	3.86
	20150216_20180107	0.14	3.50
	20150216_20180119	0.14	4.24
	20150216_20180212	0.13	3.94
	20150511_20190114	0.11	6.35
	20150511_20190303	0.11	5.90
	20151026_20170301	0.12	3.72
	20151119_20190126	0.12	2.09
	20160106_20180308	0.12	1.86

	20160130_20161113	0.15	2.08
	20160130_20181127	0.12	1.58
	20160130_20190102	0.12	1.56
	20160318_20190126	0.11	3.29
	20160318_20190303	0.11	2.73
	20161231_20190114	0.14	2.29
	20171226_20190102	0.16	1.45
	20180308_20181127	0.14	1.98
	20180308_20181209	0.14	2.65

Table S2 Best-fitting characteristic decay times for timeseries differences taken from multiple swaths at variable distances from the fault.

τ (days)	0-1 km swath	1-2 km swath	1-3 km swath	3-5 km swath
Northern Segment	3500	2000	1500	1500
Central Segment	70	200	250	500
Southern Segment	150	200	250	1000

Text S1. The influence of profile length and fitting method choices for surface creep rate estimation

The estimated surface creep rate depends on a number of choices. One of the important factors is the choice of the profile section on each side of the fault that is used in the cross-fault offset estimate, including how much data we mask out near the fault trace and the total length of the velocity profile. We explored multiple choices of profile settings varying the mask width and profile-line length from 0.5-1 km, 0.5-1.5 km, 0.5-2 km, 1-2 km, to 1-3 km. The inverted surface creep rates along the XSF using the listed settings are shown in Figure S1 (a), with selected fitting examples shown in Figure S1 (b). The result of all profile length choices shows a similar overall along-strike pattern. The choice of how wide a zone to mask out near the fault significantly influences the creep rate estimation. By changing the mask width from 0.5 km to 1 km, the creep rate increases by as much as 50% at ~175 km along strike section. On the other hand, the change of total length of the profile lines does not alter the result that much. This is not surprising because we mainly care about the near fault velocity differences and based on our method stated in the main text, near-fault pixels would have more influence on the creep rate estimate.

Another factor that could affect the estimated creep rate is how the potential step is determined across the fault. We compared two different ways in our study and show the corresponding results in Figure S1 (c). The first scheme is to conduct a linear regression of the selected length on each side of the fault, and take the modeled velocity difference at the line-segment tips (solid lines in Figure S1 (c); e.g., x=±0.5km). The second scheme is simply averaging the velocities of the near-fault data patches and then taking the difference (dashed lines in Figure S1 (c)). Distributions of the along-strike creep rate estimated by the two schemes have a systematic shift of ~1 mm/yr.

We ultimately adopted the 0.5~1.5km profile length and the linear-fitting method as our preferred choice, which keeps a balance between the signal to noise ratio, creep rate estimation bias, and location ambiguity of fault trace.

Figure S1

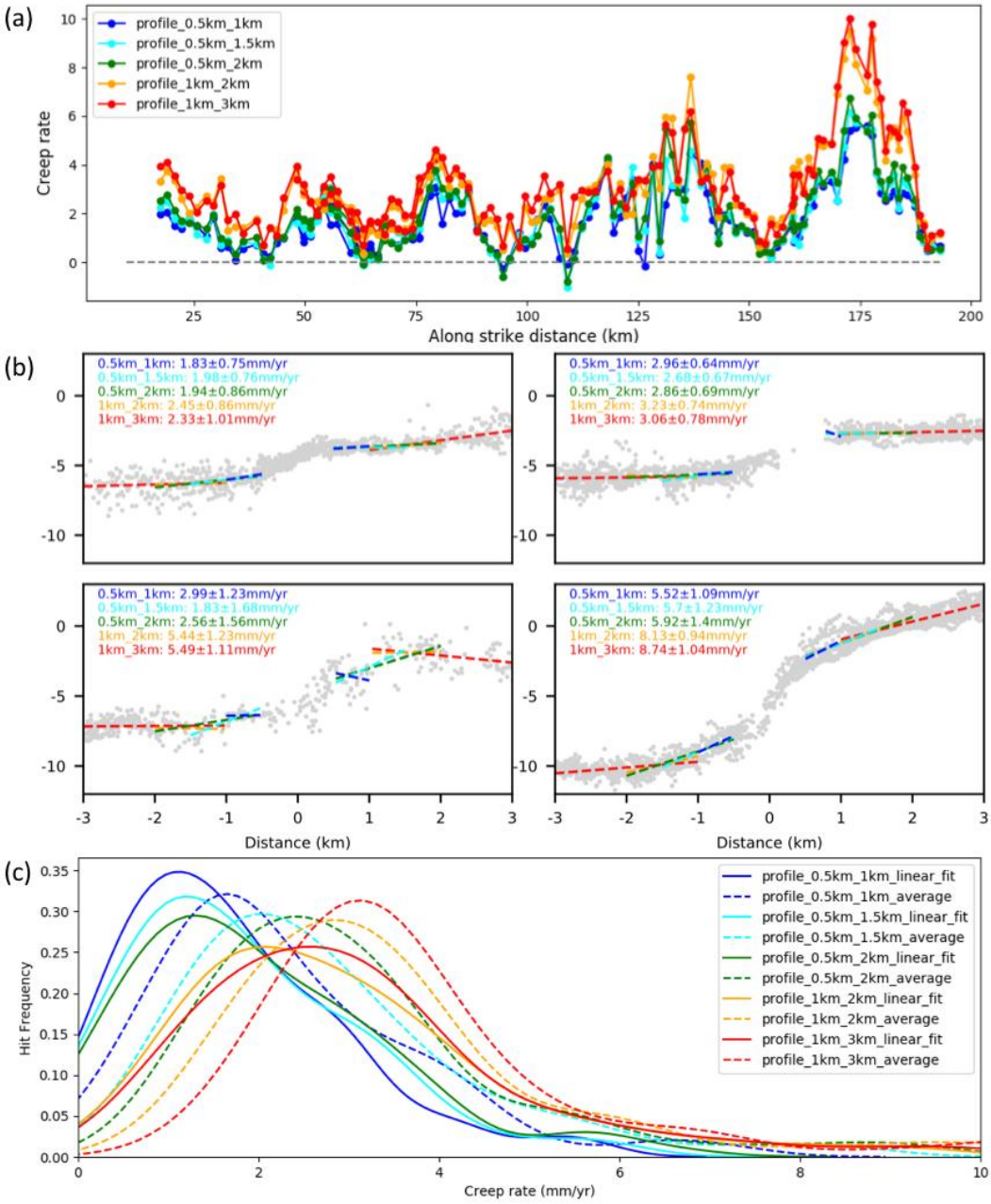

Figure S1. (a) Comparisons of surface creep rates along the XSF estimated by multiple profile settings. (b) Examples of fault-perpendicular velocity profiles and their fittings for different profile lengths. (c) Distributions of the along-strike surface creep rate estimated by either averaging or linear fitting of the profile sections for each profile length.

Figure S2

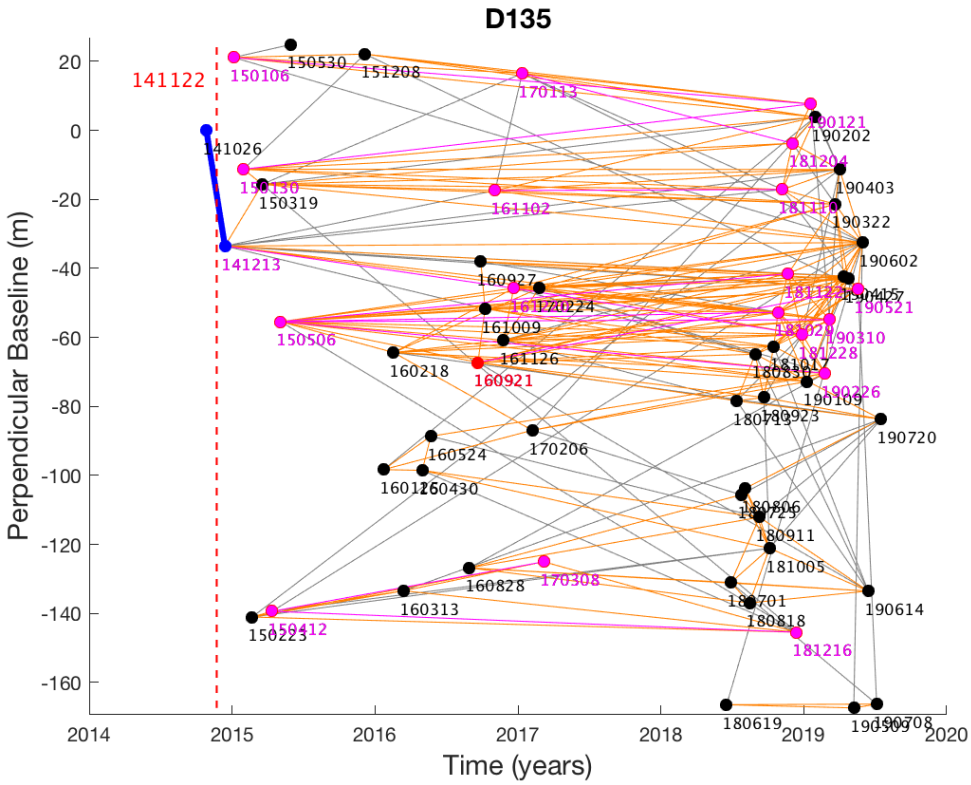
D135
141122
Perpendicular Baseline (m)
Time (years)
20
0
-20
-40
-60
-80
-100
-120
-140
-160
2014
2015
2016
2017
2018
2019
2020
150530
151208
150106
170113
190121
190202
141026
181204
190403
150319
161102
190322
141213
190602
160927
190521
170224
161009
150506
190310
160218
161126
160921
190109
190720
160524
170206
160430
180911
181005
160828
170308
180701
190614
160313
180818
150223
181216
180619
190708

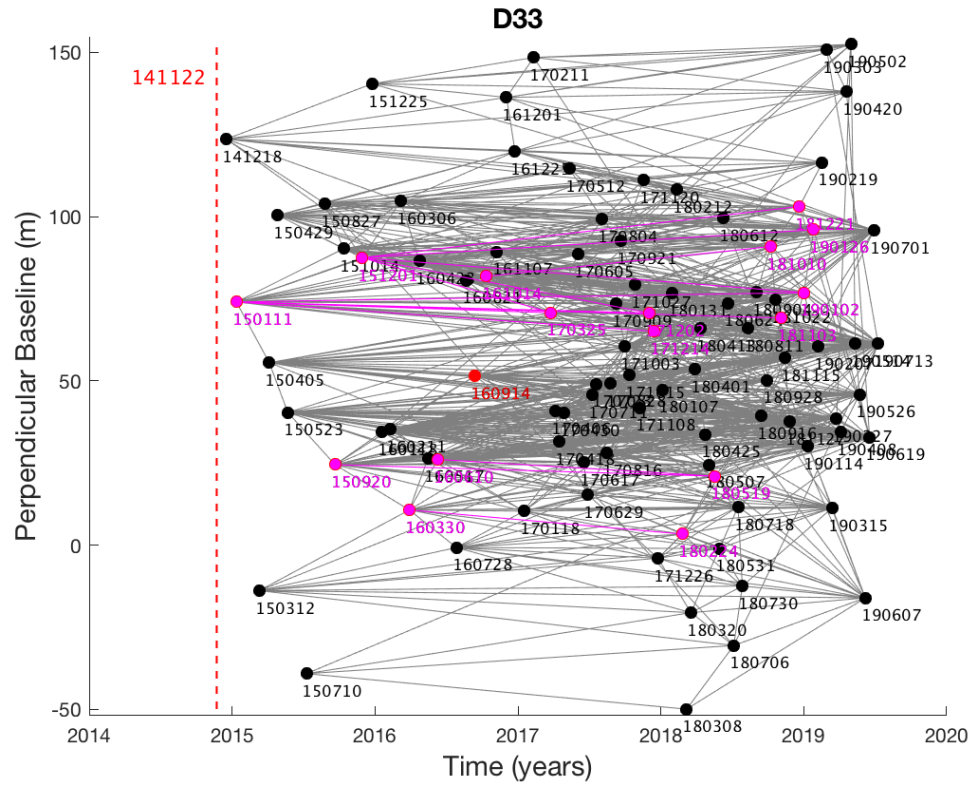
D33
141122
Perpendicular Baseline (m)
Time (years)
150
100
50
0
-50
2014
2015
2016
2017
2018
2019
2020
170211
190502
151225
190420
161201
141218
190219
150827
160306
150429
180612
190701
161107
170605
150111
150405
160914
150523
190526
150920
160330
170118
190315
160728
171226
180531
150312
180730
190607
180320
180706
150710
180308

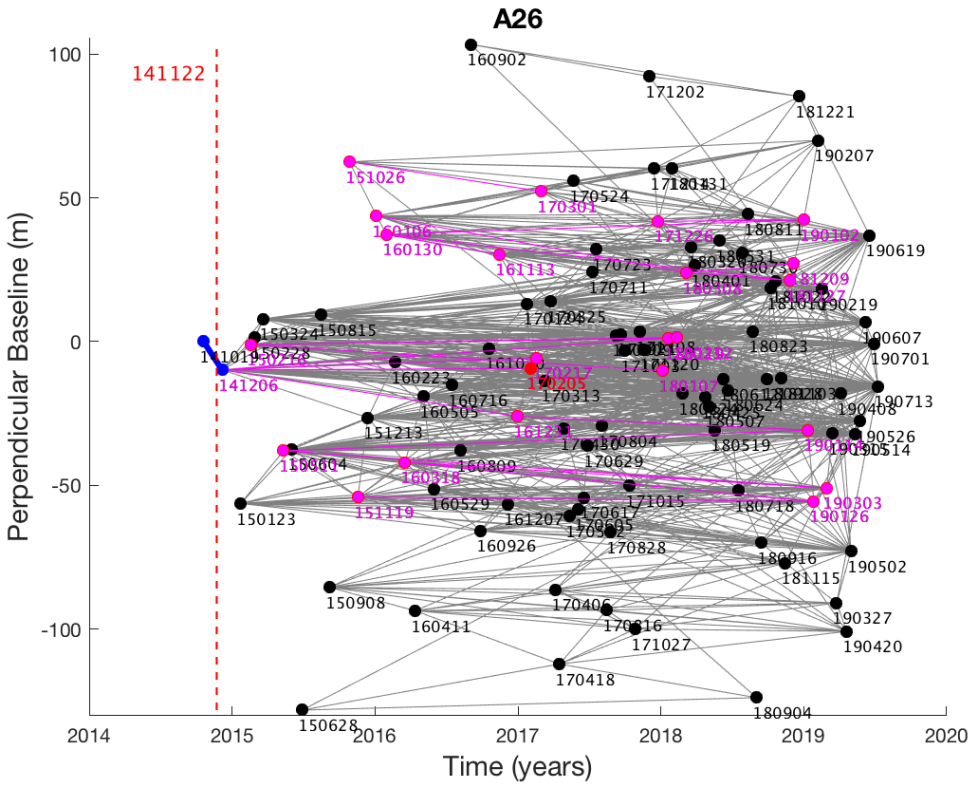

71

72 **Figure S2. (a)-(c)** Interferogram network for tracks D33, D135 and A26 for co- and
73 postseismic deformation used in this study. Each acquired scene is marked as a solid
74 circle and all interferograms generated in this study are marked as lines. The selected
75 interferograms for the velocity map formation (Figure 4) are colored in magenta. For
76 D135, interferograms with STD<3 that are used in the timeseries analysis are colored in
77 orange. The coseismic interferograms are shown by bold blue lines. The date of the
78 Mw5.9 Kangding earthquake is marked by red dashed line.

79

Figure S3

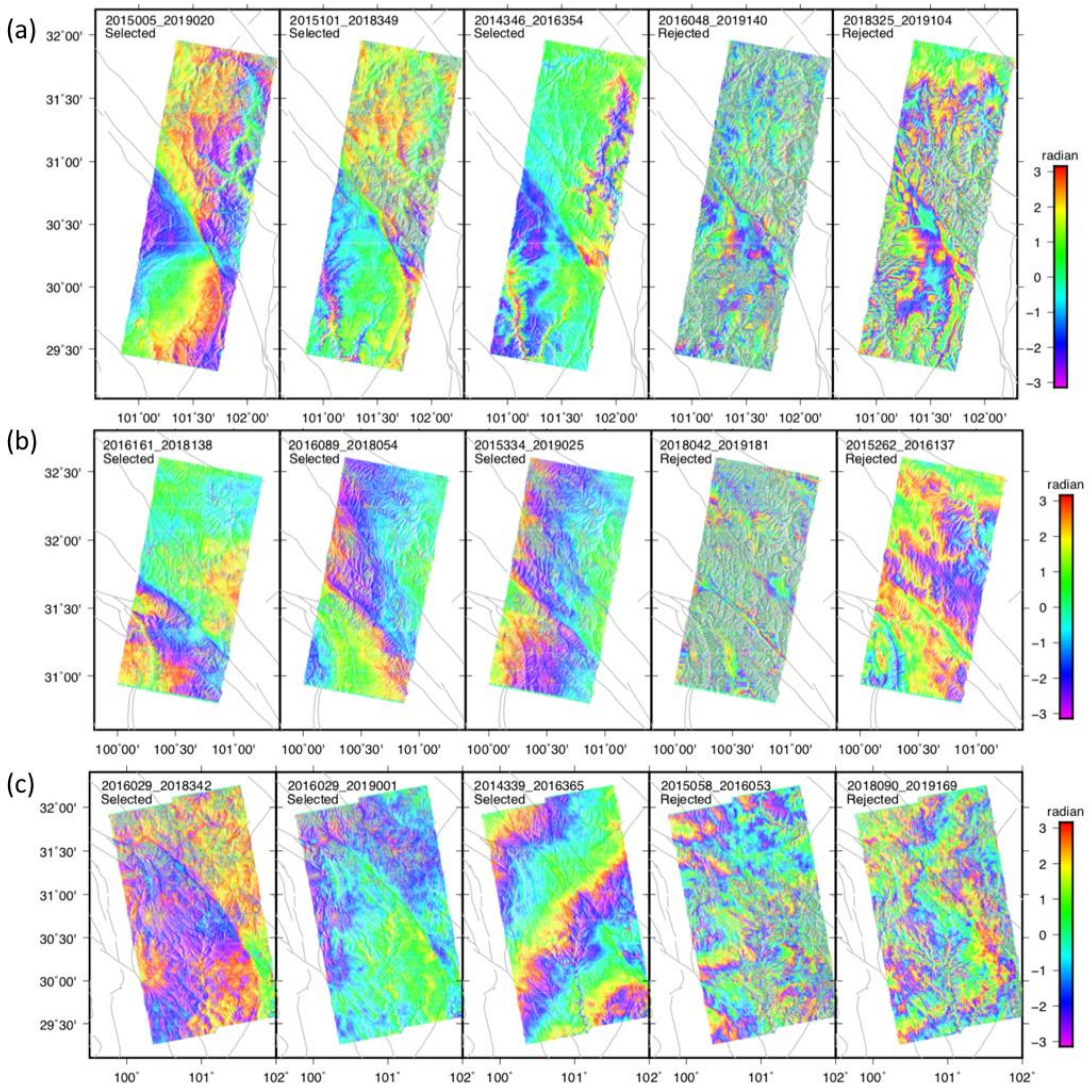

Figure S3. Examples of selected and rejected interferograms for (a) descending track T135F2, (b) descending track T33, and ascending track T26. Dates used to form the interferograms are shown at the top of each panel.

Figure S4

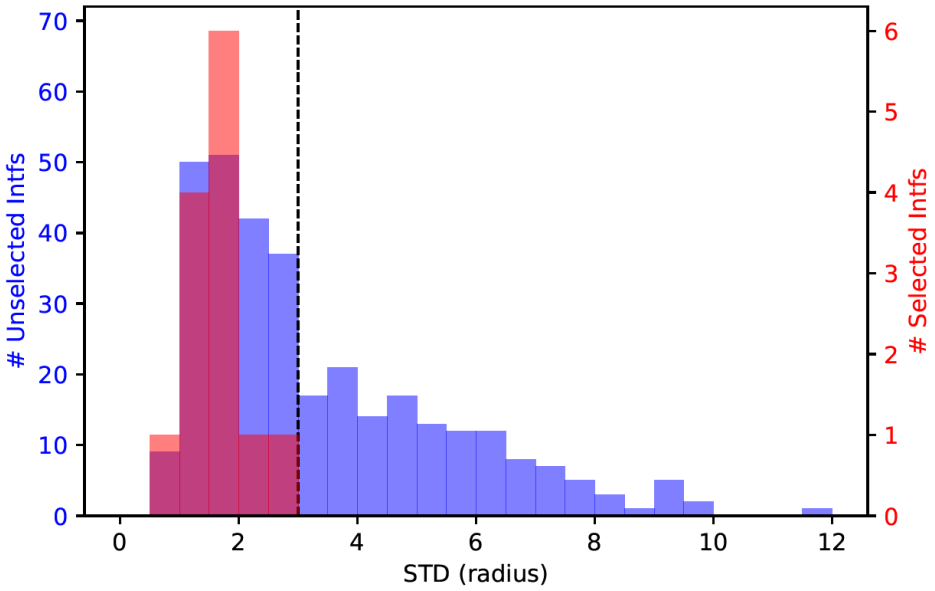

Figure S4. Histogram of the standard deviation (STD) of selected and rejected unwrapped interferograms for D135F2.

Figure S5

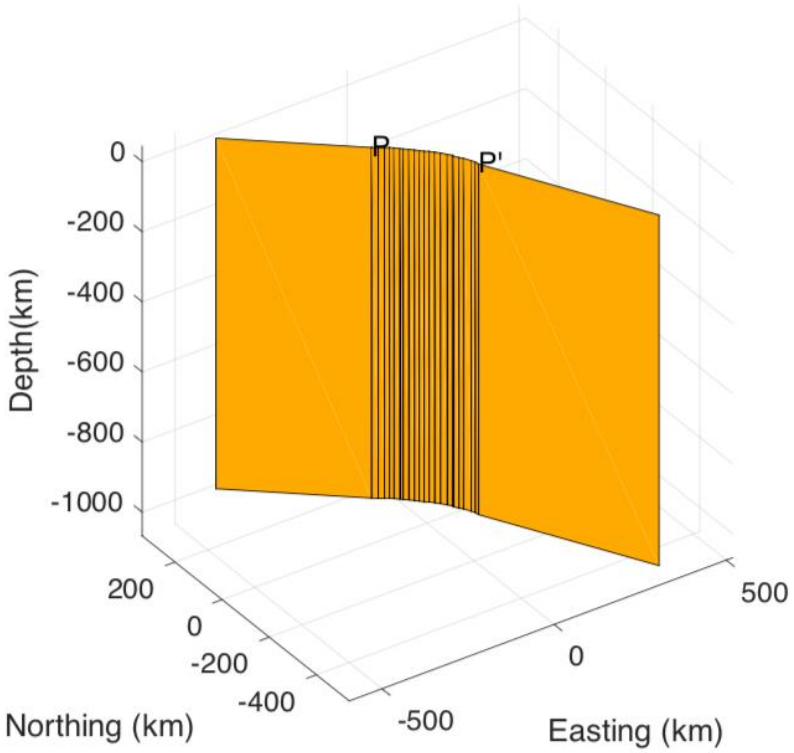

Figure S5. Geometry of the deep dislocation model. PP' indicates the extent of the shallow slip model. The deep dislocation model consists of a series of 1000-km-wide dislocations slipping at 12.11 mm/yr below 12 km along the XSF, with lateral

96 extensions that go far beyond the fault tips.

Figure S6

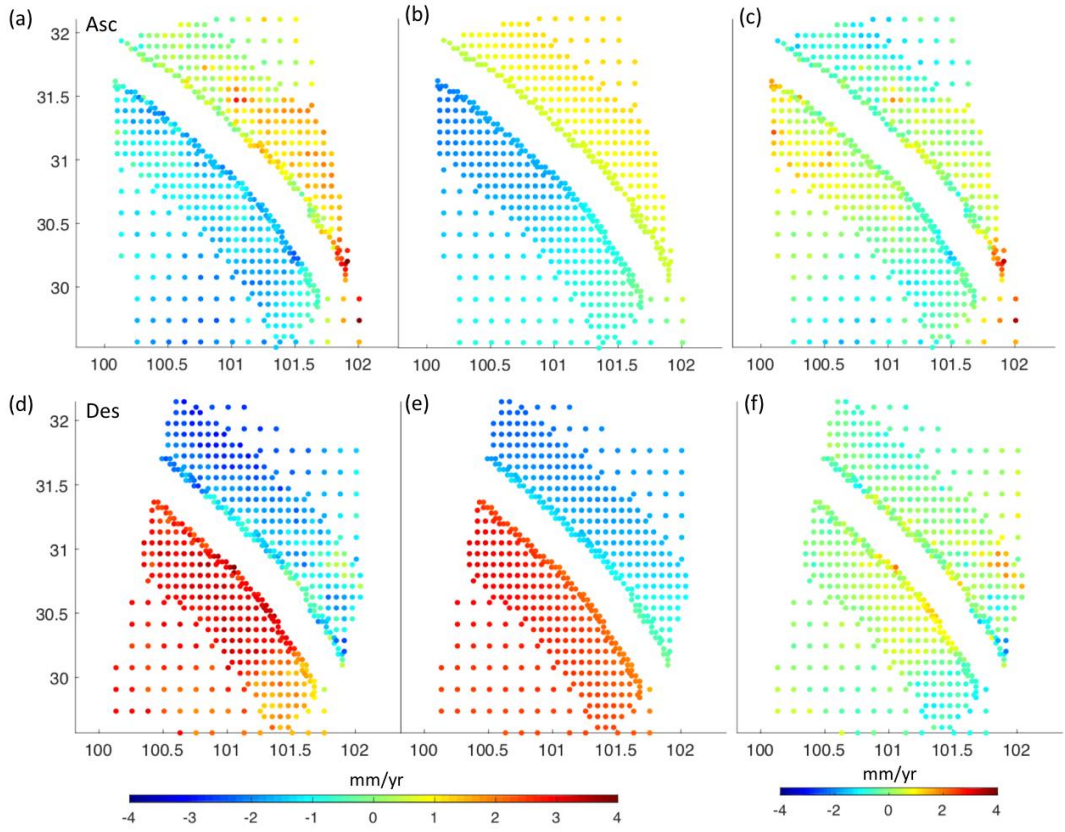

Figure S6. Comparison of downsampled observed and modeled long-wavelength LOS velocities from ascending and descending Sentinel-1 viewing geometries. The deep-dislocation model geometry is shown in Figure S5. (a-c) are observed, modeled, and observed-minus-modeled residuals for ascending track 26. (d-f) are corresponding maps for descending orbit 135. Note that near-fault data within 15 km of the XSF are masked out when inverting for the deep slip rate of 12.11 ± 0.68 mm/yr.

Figure S7

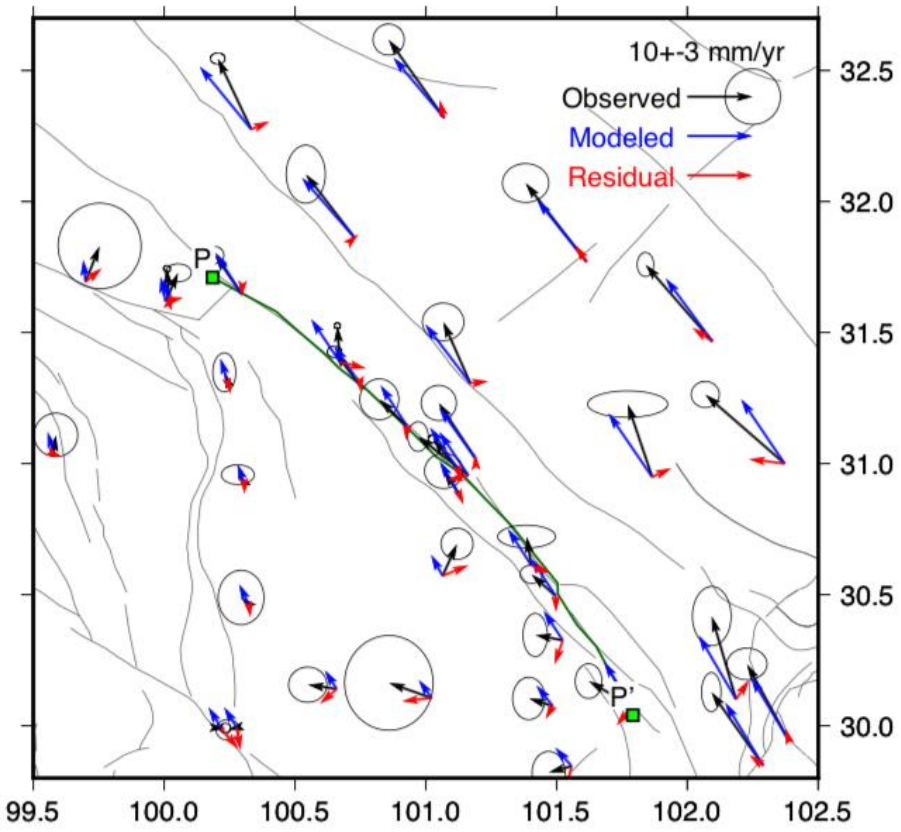

Figure S7. Comparisons of observed and modeled GPS velocities using the derived deep dislocation model. Black, blue and red vectors show the observed, modeled, and observed-minus-modeled residual velocities, respectively. GPS velocities are relative to Yajiang sub-block and tipped with 95% confidence ellipses (Zheng et al., 2017). The modeled fault trace is shown in dark green lines.

Figure S8

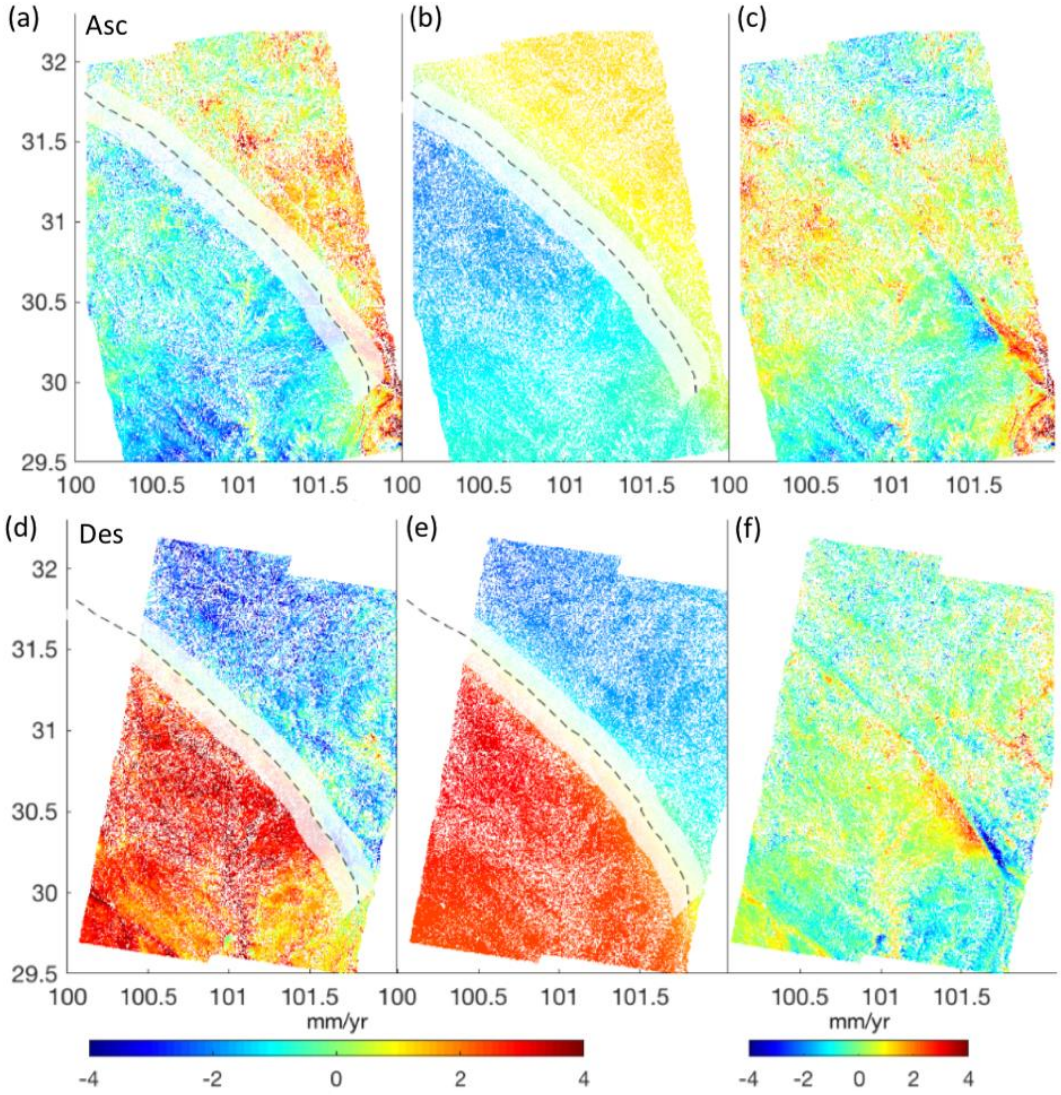

Figure S8. Deep dislocation model and residual maps. (a-c) are observed, modeled, and residuals for ascending track 26 (same as in Figure S6 but shown without downsampling used in the model inversion). (d-f) are corresponding maps for descending orbit 135. Note that data from within 15 km of the fault are masked out when inverting for the deep slip rate but are shown in the residual maps. The residual velocities shown in (c) and (f) are used to invert for the aseismic slip distribution above 12 km (Figures 7 and 8).

Figure S9

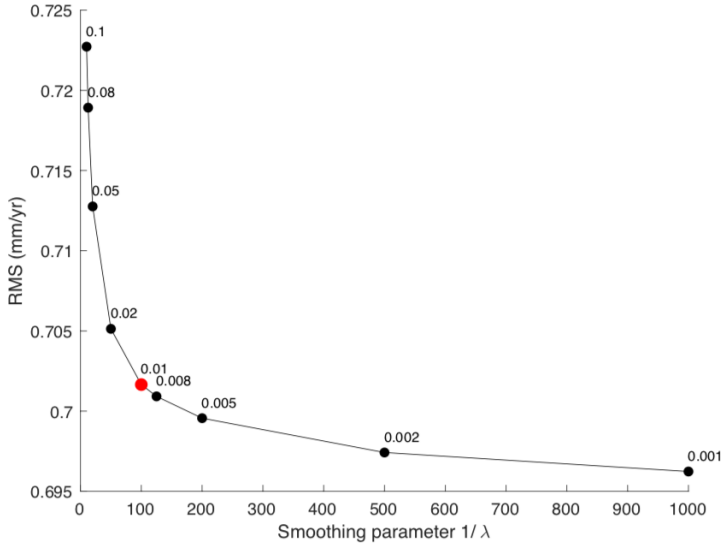

Figure S9. Trade-off curve for smoothing parameters of the shallow slip inversion. We use 0.01 as our preferred smoothing parameter in the inversion.

Figure S10

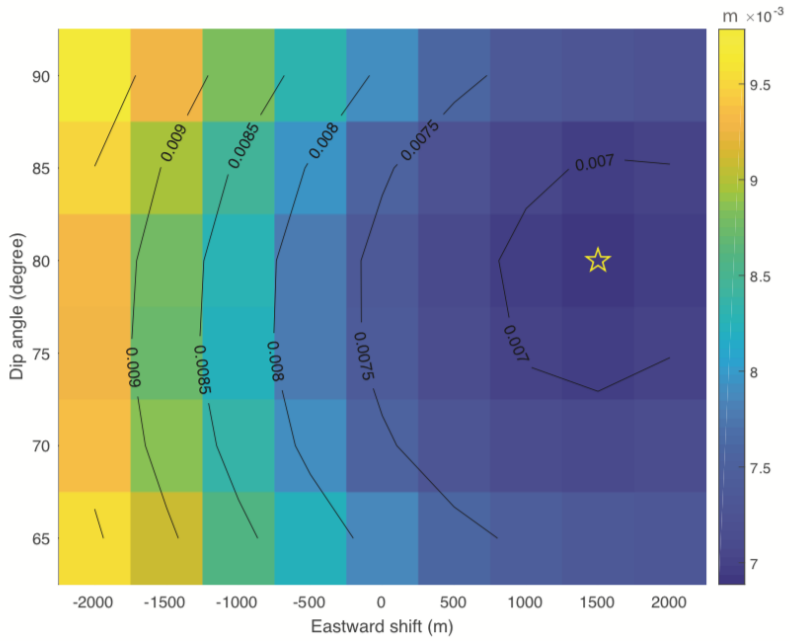

Figure S10. Residual (RMS) plot for the coseismic slip model for ranges of locations of the surface trace and variable dip angles of the Mw5.9 rupture plane.

Figure S11

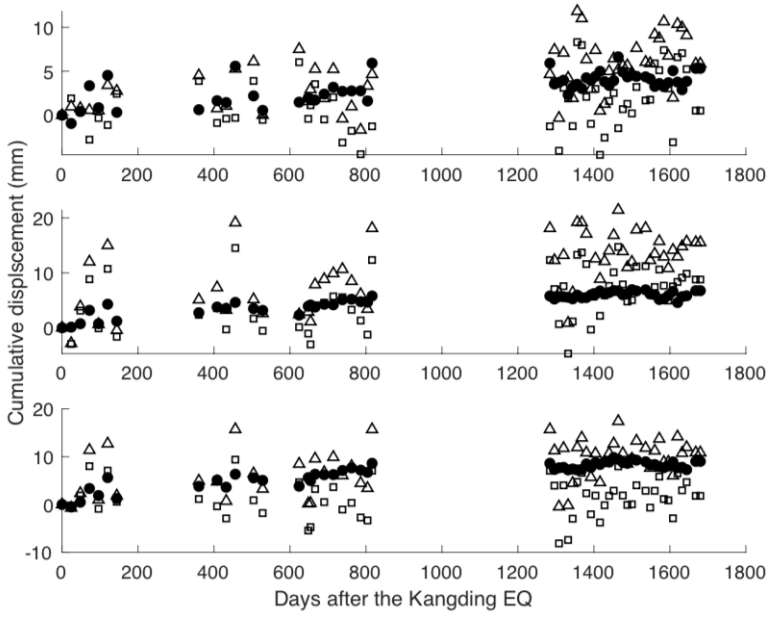

Figure S11. Stacked averaged LOS timeseries and the cross-fault timeseries differences for descending track 135 along the (a) northern, (b) central and (c) southern fault sections. Black triangles and squares show the averaged cumulative displacement at patches west and east of the fault, respectively. Black solid circles show their cross-fault differences.

Figure S12

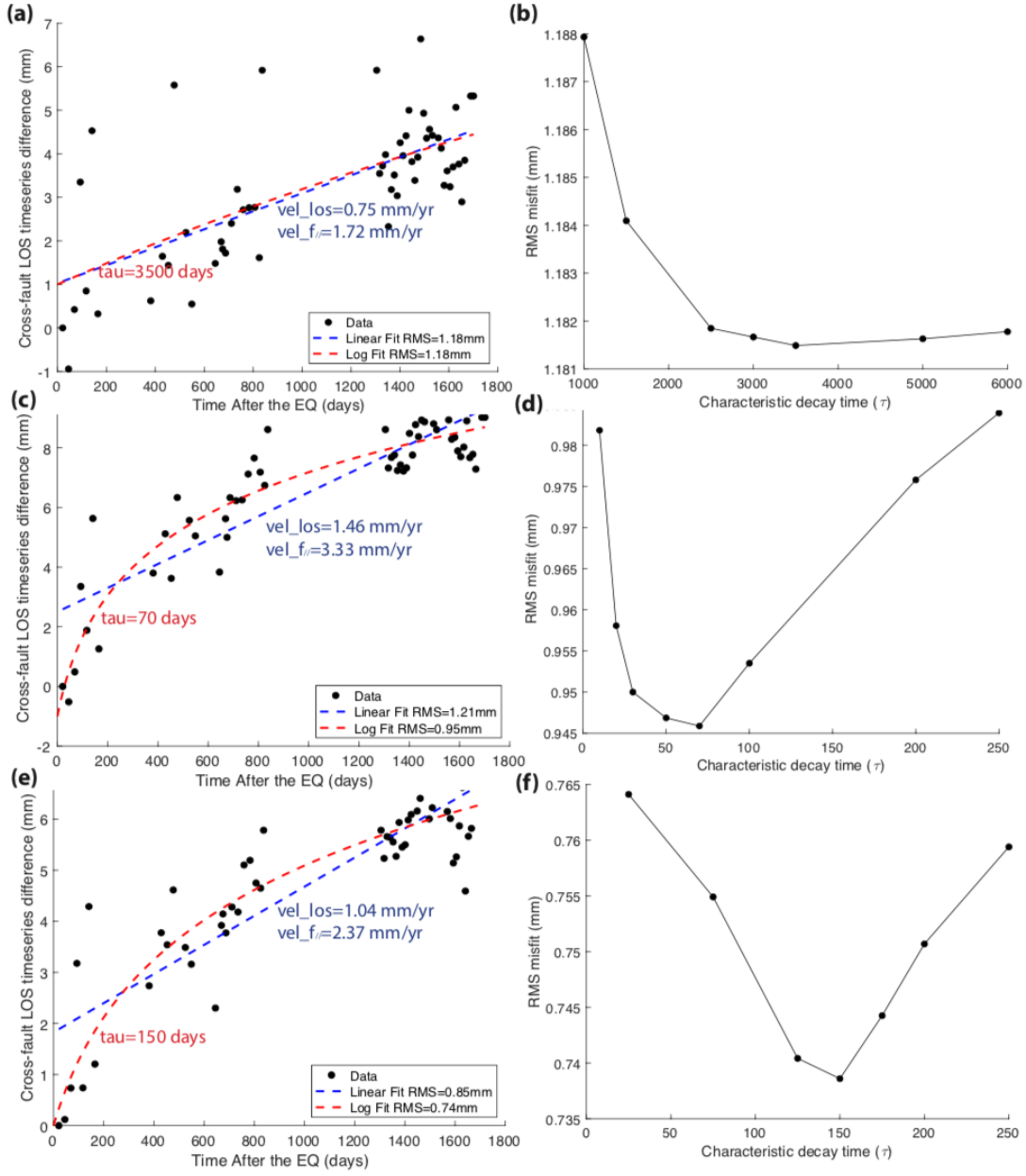

Figure S12. Stacked averaged LOS cross-fault timeseries differences (see Figure S11) along the (a) northern, (c) central and (e) southern fault sections with the linear and log-decay fittings that minimize the RMS misfit. Relationship between the RMS misfit and chosen characteristic decay time (tau) for the corresponding segments are shown in (b), (d) and (f).

Figure S13

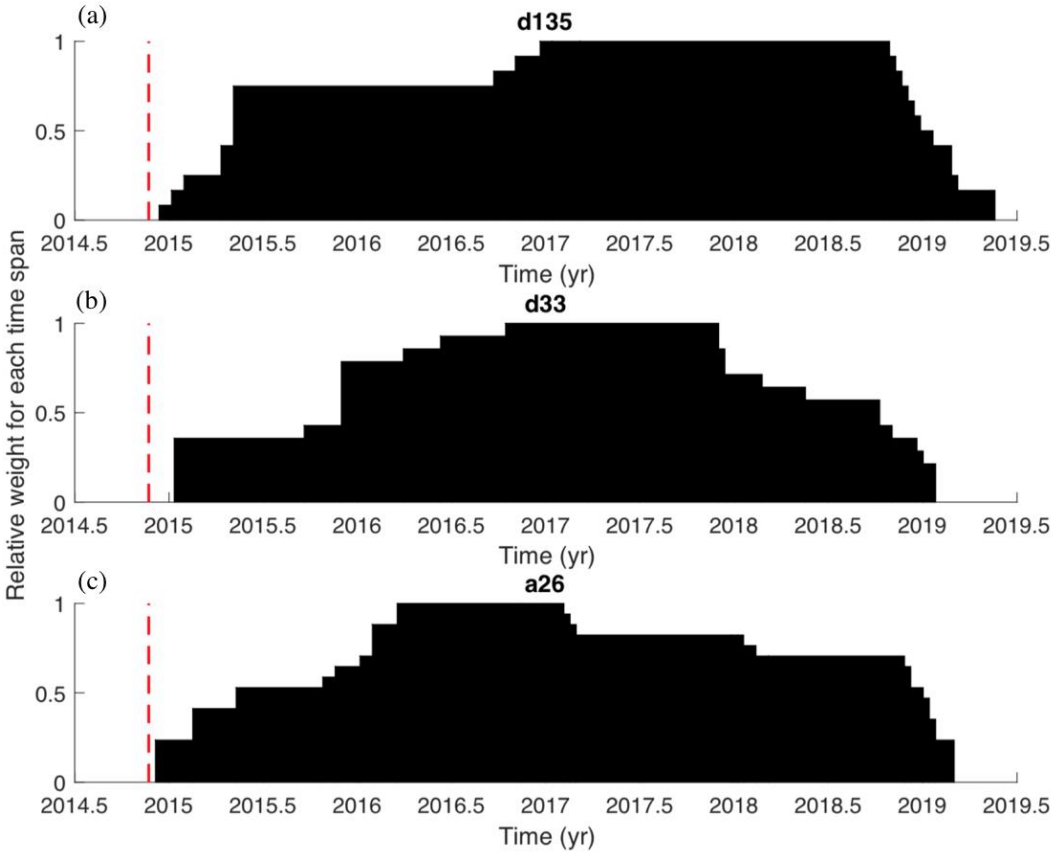

Figure S13. The normalized weight of time-spans that are used in the average velocity map formation for (a) descending track 135, (b) descending track 33, and (c) ascending track 26.

Figure S14

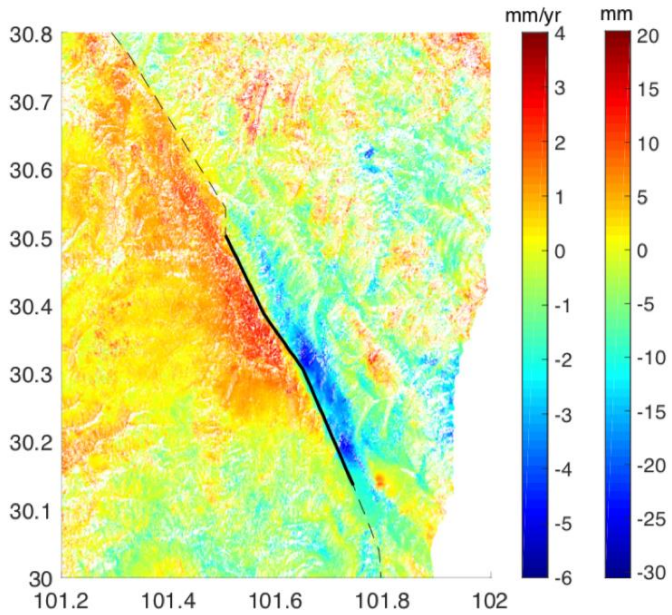

Figure S14. A zoom-in map of the average velocity map of descending track 135. The data and region are outlined in Figure 8f. Colorbar to the left shows the LOS velocity and colorbar to the right shows the reconstructed cumulative displacement map from the average velocity map by multiplying the average velocity map with a scaling factor of 5.09.

Figure S15

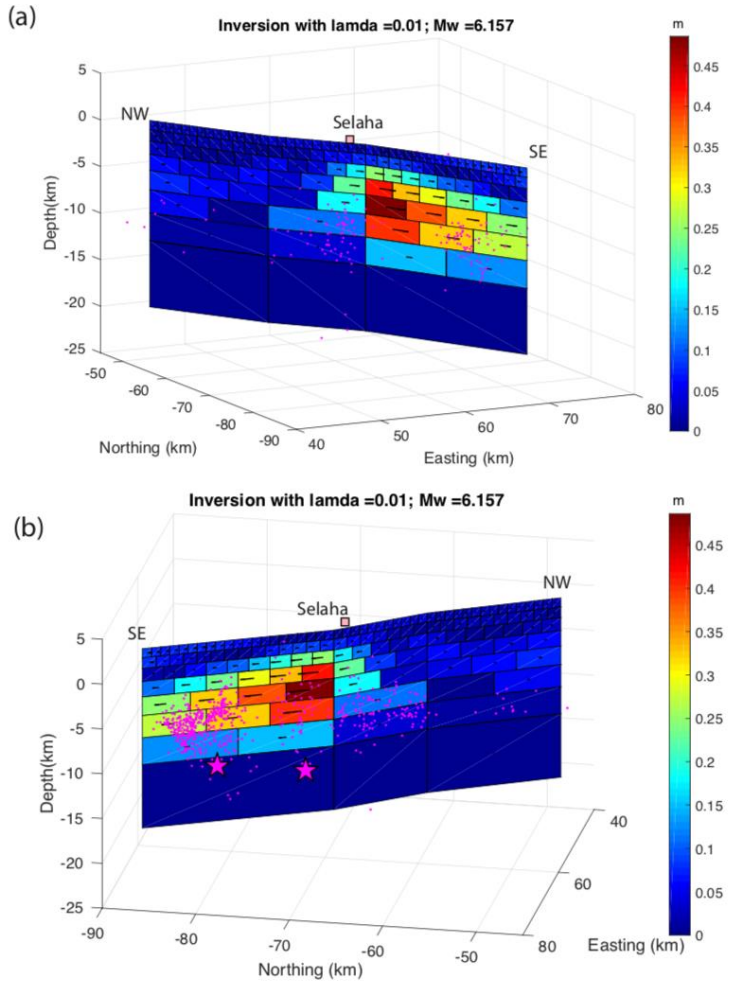

Figure S15. Simplified coseismic slip model using the fault geometry of the SE section of the coupling model. Magenta stars show the hypocenters of the two largest events and magenta dots show the first 24 days of relocated aftershocks of the 2014 Kangding earthquake sequence (Fang et al., 2015).

Figure S16

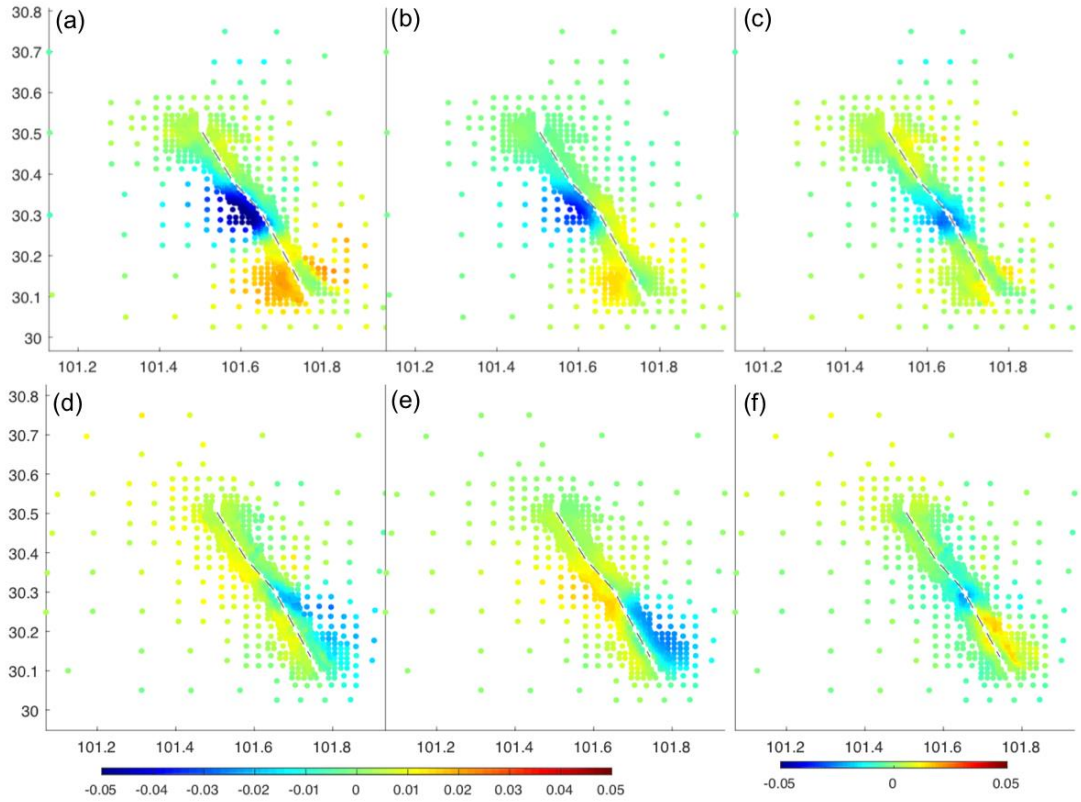

Figure S16. Comparison of observed and modeled coseismic deformation of Kangding earthquake from both ascending and descending Sentinel-1 geometries using the fault geometry of the SE section of the coupling model. (a-c) are observed, modeled, and observed-minus-modeled residuals for ascending track 26. (d-f) are corresponding maps for descending orbit 135. Black dashed lines indicate surface traces of the fault rupture model in Figure S15.